Modelling of offshore pile driving noise using a semi-analytical variational formulation

Qingpeng Deng[a,1], Weikang Jiang[a], Mingyi Tan[b], Jing Tang Xing[b]

[a]*Institute of Vibration, Shock and Noise,*

Shanghai Jiao Tong University, 800 Dongchuan Road, 200240 Shanghai, China

[b]*Fluid Structure Interactions Group, FEE,*

University of Southampton, Southampton SO16 7QF, United Kingdom

Corresponding author: Weikang Jiang

E-mail address: wkjing@sjtu.edu.cn

Postal address: *Room 820, Building A, Institute of Vibration, Shock and Noise,*

800 Dongchuan Road, 200240 Shanghai, China

Phone number: 0086 (0)21 34206332 Ext. 820

Abstract

Underwater noise radiated from offshore pile driving got much attention in recent years due to its threat to the marine environment. This study develops a three-dimensional semi-analytical method, in which the pile is modeled as an elastic thin cylindrical shell, to predict vibration and underwater acoustic radiation caused by hammer impact. The cylindrical shell, subject to the Reissner-Naghdi's thin shell theory, is decomposed uniformly into shell segments whose motion is governed by a variational equation. The sound pressures in both exterior and interior fluid fields are expanded as analytical functions in frequency domain. The soil is modeled as uncoupled springs and dashpots distributed in three directions. The sound propagation characteristics are investigated based on the dispersion curves. The case study of a model subject to a non-axisymmetric force demonstrates that the radiated sound pressure has dependence on circumferential angle. The case study including an anvil shows that the presence of the anvil tends to lower the frequencies and the amplitudes of the peaks of sound pressure spectrum. A comparison to the measured data shows that the model is capable of predicting the pile driving noise quantitatively. This mechanical model can be used to predict underwater noise of piling and explore potential noise reduction measures to protect marine animals.

Keywords: Structural-acoustic modeling, Underwater noise, Pile driving, Cylindrical shell

1. Present address: *Institute of Vibration, Shock and Noise, Shanghai Jiao Tong University, 800 Dongchuan Road, 200240, Shanghai, China*

1. Introduction

There is a rapid increase of offshore constructions over the world in the recent years, such as wind turbine installations, petroleum and gas platforms, artificial islands and oversea bridges. These constructions produce severe underwater noise pollution which has raised serious concerns from environmental protection organizations and academic world. Pile-driving noise is generally considered as the most severe underwater noise which would harm or even kill marine animals inhabiting around piling sites, such as fishes, dolphins and whales [1-3].

It is necessary to establish an accurate and realistic mechanical model to understand the mechanism and propagation characteristics of the underwater noise radiated from pile driving. In order to predict the sound radiation accurately, the complex fluid-structure interactions between the pile wall and its surrounding fluid must be taken into consideration. The compressibility of the fluid alters the effective stiffness of the system and the fluid exerts inertial loading on the shell, which results in significant changing of the resonant frequencies. The fluid-structural interaction problems of circular cylindrical shells partly or completely submerged and subjected to either external or internal fluid have caused interest to scientists. Green function and Fourier integral technique were used by Stepanishen [4] to evaluate the radiated loading and radiated power from a non-uniform harmonically vibrating surface on an infinite cylinder which was in contact with a fluid medium. The effect of fluid loading on the vibration and sound radiation of finite cylindrical shells has been studied by the authors [5, 6] who used in-vacuo shell modes to present the structural vibration field and, in order to compute the sound field, extended the finite shells to infinity at both ends by rigid co-axial baffles. The low-frequency structural and acoustic responses of a fluid-loaded cylindrical shell with structural discontinuities, corresponding to ring stiffeners and bulkheads, were investigated by Caresta and Kessissoglou [7]. The work was then extended to consider the sound radiation from a more detailed submarine structure in which the cylindrical shell is closed by truncated conical shells and circular plates [8]. Kwak, et al. [9] investigated the natural vibration characteristics of a hung clamped-free cylindrical shell partially submerged in fluid based on the added virtual mass approach. Detailed discussions of the dynamics of coupled fluid-shells can be found in [10-13].

The sound radiation of cylindrical pile has been getting increasing attention in recent years. The Finite Element Method (FEM) is a common method for establishing pile-driving models. Axisymmetric FEM models (two-dimensional models) are frequently used because they are computationally efficient. Axisymmetric FEM models were established to analyze underwater noise of pile driving, in which perfectly matched boundary conditions for water and sediment were applied to truncate the domain and emulate the Sommerfeld radiation condition [14, 15]. The discretization of the sound field at long distances by FEM models is impractical because the total number of unknowns of the system is limited due to computational reasons. It is common to use a hybrid scheme consisting of a discretized FEM model for pile and its surroundings combined with an approximate propagation model for long ranges. A combination of a FEM model and a parabolic wave equation (PE) model was used by Reinhall and Dahl [16]. A similar combination was also established by Kim, et al. [17] who used a modified version of the Monterey-Miami Parabolic Equation (MMPE) to predict long range noise propagation. Lippert, et al. [18] combined a FEM model with a head wave model to forecast the noise of pile driving. In their subsequent publication the significance of soil parameter uncertainties for the underwater noise is investigated based on the wave number integration scheme combined with an axis-symmetric FE model [19]. The model of Fricke and Rolfes [20] included a

FEM model for the computation of the vibration and the radiated sound of the pile, a parabolic model for the long-range propagation and an analytical model for hammer force estimate. Semi-analytical models are also used in predicting offshore pile driving noise. A model of a semi-infinite tubular pile was presented by Hall [21] to predict the peak pressure of the radiated sound pulse by linking with both depth-independent vibration and depth-dependent vibration. The model was then extended to compute the radiated sound of a pile with finite length in combination with the Ray theory which deals with the sound propagation in water and soil in a simple manner [22]. Another semi-analytical model was established by Tsouvalas and Metrikine [23] who expressed the shell displacements as the summation of the in-vacuo shell modes and expressed the sound pressure in fluid field as the summation of a set of analytical functions.

In this study a linear semi-analytical model is developed to predict pile-driving noise based on a modified variational methodology, in which the shell is divided into several sub-shells along the axial direction and the effect of water and soil is taken into account as virtual work acting on the sub-shells. The mechanical model presented in the paper is similar to the previous one introduced by Tsouvalas and Metrikine [23]. What the authors do in this paper is to propose a new approach to solve the responses of the model. In addition, we expand upon sound propagation characteristics, pressure distributions and reveal the influence of the non-axisymmetric impact force and the anvil on the sound radiation. Compared to the approach used in [23], the effort to seek in-vacuo shell modes is avoided, which makes it capable of dealing with piles with more complex boundary conditions in which, for example, the pile anvil, cushions and the pile footing (usually a conical shell) are connected to the pile ends.

The paper is arranged as follows. In the next section, the description and basic assumptions of the model are given. In Sec. 3, the basic theory of the methodology is introduced and the governing equations of the motion of the pile are derived. Sec. 4 gives a description of the sound propagation characteristics based on the dispersion relation curves of the pressure modes, followed by a numerical case with an axisymmetric hammer force in Sec. 5 and a numerical case with a non-axisymmetric hammer force in Sec. 6. The influence of the pile anvil on the sound radiation is investigated in Sec. 7. Sec.8 gives a comparison between modelling values and tested data, before the conclusions are summarized in Sec. 8.

Nomenclature

c_x , c_θ , c_r	equivalent viscous soil damping coefficients along the three coordinate directions
E_{soil}	elastic modulus of soil
I	the total number of shell segments
I_e	the number of the shell segments in contact with exterior fluid
j	Imaginary unit: $j = \sqrt{-1}$
k_x, k_θ, k_r	equivalent soil spring coefficients along the three coordinate directions
m	orders of axial displacement functions
M	the highest order of the axial displacement functions
n	circumferential orders of displacement functions and pressure modes

N	the highest order of the circumferential displacement functions
p	index of the wavenumbers of the sound pressure
x_i	minimal vertical coordinate of fluid-structure interface on the i^{th} submerged shell segment
x_{i+1}	maximal vertical coordinate of fluid-structure interface on the i^{th} submerged shell segment
x_{s1}	minimal vertical coordinate of shell-soil interface on each shell segment beneath the seabed
x_{s2}	maximal vertical coordinate of shell-soil interface on each shell segment beneath the seabed
μ_{soil}	Poisson ratio of soil material
ρ_{soil}	density of soil
β_{soil}	equivalent damping ratio of soil
ζ	the ratio of the impedance of the seabed to characteristic impedance of the fluid
$\boldsymbol{C}_e$, $\boldsymbol{C}_i$, $\boldsymbol{C}_{\text{soil}}$	coupling matrixes introduced by exterior fluid, interior fluid and soil, respectively
$\boldsymbol{F}(\omega)$	generalized force vector
$\boldsymbol{K}$	main structural stiffness matrix
$\boldsymbol{K}_\lambda$	stiffness matrix incorporated by interface forces and moment
$\boldsymbol{K}_\kappa$	stiffness matrix incorporated by least-squares weighted parameters
$\boldsymbol{M}$	structural mass matrix
$\boldsymbol{q}(\omega)$	generalized coordinate vector
$\delta(\ )$	the variation of ( )
$(\ )^{\mathrm{T}}$	the transpose of ( )

2. Model description

The schematic diagram of the pile-driving model is shown in Fig. 1. The model assumptions are similar with those introduced in [23]. The assumptions are listed as following:

(1) The pile is modelled as a thin elastic cylindrical shell with finite length and constant thickness. The motion of the shell is subject to Reissner-Naghdi's thin shell theory [24].

(2) The seawater inside and outside the pile is assumed to be compressible and inviscid fluid with constant sound velocity and density. There is no flow in the fluid field.

(3) The influence of the air on the vibration of the pile is neglected.

(4) The sea surface (fluid-air interface) is assumed to be a pressure release boundary on which the sound pressure vanishes.

(5) The shell and the fluid field are required to satisfy the normal velocity continuity condition on the shell-fluid coupling interface.

(6) The seabed is assumed to be either an acoustic rigid boundary or an acoustic impedance boundary.

(7) The soil surrounding the pile is modelled as uncoupled distributed springs and dashpots in three directions.

(8) The impact force of the hydraulic hammer is modelled as distributed force acting on the circumference of pile top.

The constants $E, \mu, \eta, \rho_s, L, h$ and R correspond to the modulus of elasticity, Poisson's ratio, structural loss factor, density, length, thickness and radius of the mid-surface of the cylindrical shell, respectively. c and ρ_f are the sound velocity and density of the seawater, respectively. The pile is filled by interior fluid at $x_{is} < x < x_b$ and surrounded by exterior fluid at $x_{es} < x < x_b$.

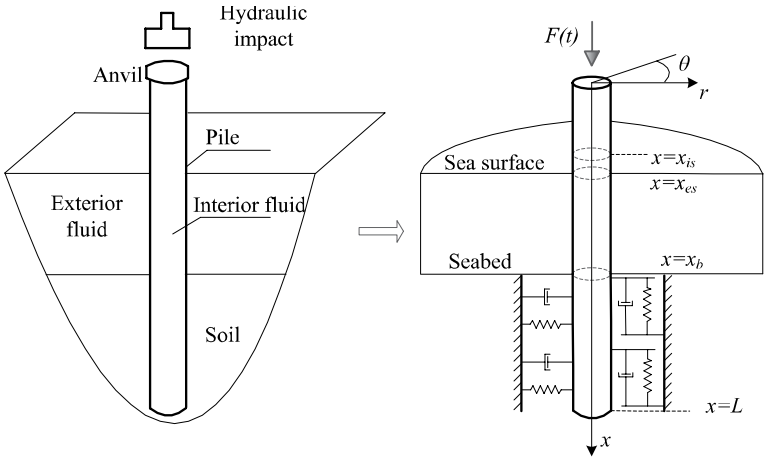

Fig. 1. Pile-driving model

3. Basic theory

A linear 3D semi-analytical mechanical model is established, in which the circular cylindrical tubular pile is divided into a number of shell segments along the symmetrical axis. A modified variation methodology is used to derive the mathematic equations governing the motion of the pile. The displacements of the shell segments are expressed as summation of a set of admissible displacement functions. The sound pressure in both exterior fluid domain and interior fluid domain is expressed as the summation of a set of analytical functions weighted by the generalized coordinates of the shell displacements. The soil is modelled as uncoupled distributed springs and dashpots in three directions. The coupling effects of fluid and soil on the pile are taken into consideration by incorporating corresponding virtual work into the variation equation. Linear equations in terms of generalized displacement coordinates can eventually obtained by seeking the stationary statement of the total functional.

This methodology is of advantage in several aspects. Firstly, compared to the FEM models, the discretization of the fluid volume, the approximate treatment on the truncated artificial boundaries and

approximate modeling for sound propagation in far acoustic field are altogether avoided. Secondly, a semi-analytical model is generally more computationally efficient compared to a non-axisymmetric three-dimensional FEM model for high frequency response and for longer ranges, because a large amount of fluid elements require large storage space and long computational time. Thirdly, the analytical expression of the sound pressure makes it possible to examine the influence of some parameters on the sound radiation in a qualitative manner. Additionally, compared to the method using in-vacuo shell modes to express structural displacements, the effort to seek the modes is avoided and the variational methodology leads to a solution that is generally easier to obtain than by solving the differential governing equations directly. At last, this methodology is applicable to piles with more complicated boundary conditions or attachments, such as the pile anvil, cushions and the pile footing. However, the presented model fails to model the pressure wave propagating in the bottom or layered bottoms due to the simplification treatment on the soil, and to evaluate the effects of the pressure wave passing through the water-soil interface due to the rigid seabed or impedance seabed assumption.

3.1. Shell decomposition

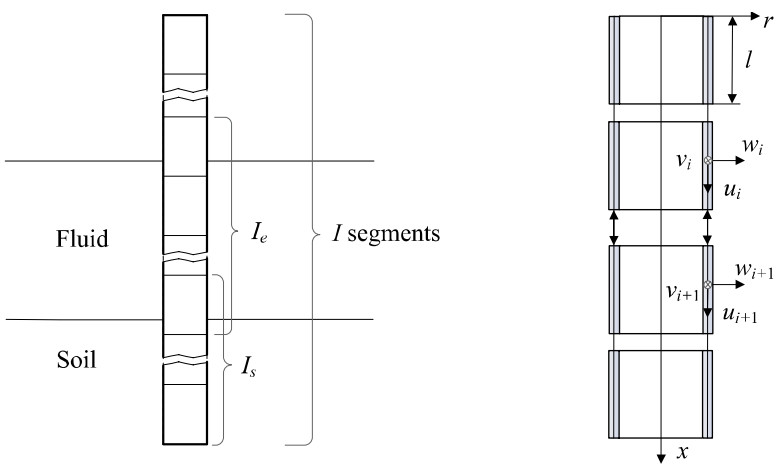

Fig. 2. Pile decomposition

A structure decomposition method with high-order of accuracy and small requirement of computational effort [25, 26] is employed here to obtain the governing equation of shell vibration, in which the cylindrical shell is divided into several shell segments along its axisymmetric axis. As shown in Fig. 2, the pile is divided equally into I sub-shells with I_e sub-shells coupled with exterior fluid and I_s coupled with soil. The method involves seeking the solution of the equation given in Eq. (1), with subscript $i = 1, 2, \cdots, I$ denoting the sequence numbers of the shell segments. $\Pi_{\lambda\kappa}$ is the interface potential defined on the common boundary of two adjacent shell segments, which incorporates the interface continuity conditions into equation. The geometrical boundaries on the two pile ends are treated as special interfaces [26]. This incorporation of the term $\delta\Pi_{\lambda\kappa}$ provides a great flexibility for the selection of admissible displacement functions, since the interface continuity conditions and geometrical boundary conditions are no longer imposed on the displacement functions, as their eventual satisfaction is implied in the variation statement. The kinetic energy T_i and strain energy U_i are all formulated based on Reissner-Naghdi's thin shell theory [24] and their expressions are given by Eq. (3) and Eq. (4), where $K = Eh/(1-\mu^2)$ and $D = Eh^3/[12\,(1-\mu^2)]$ are the membrane stiffness and bending stiffness of the shell, respectively. The modified term $\Pi_{\lambda\kappa}$ is referred to Qu's work [25]. The term δW_i is the virtual work of external force and is given in Eq. (2), where

δu_i, δv_i, δw_i are corresponding virtual displacements of the i^{th} shell segment in x, θ and r direction, respectively. $f_{u_i}, f_{v_i}, f_{w_i}$ are the distributed forces acting on the i^{th} shell in the three directions, respectively. The impact force of the hydraulic hammer, the forces of springs and dashpots and the sound pressure of the fluid are all considered as external forces. Therefore, the effects of the fluid and soil on the pile are all included in the equation in the form of virtual work.

In Sec. 5 and Sec. 6, the pile head is subject to free boundary condition, with the axial stress, circumferential and lateral shear stresses, and the bending moment being zero. The axial stress 'equals zero' in a sense that no geometrical constraint is applied in axial direction, but the axial stress does exist as the hammer imparts force to the pile head. Strictly speaking, the pile toe is a complicated boundary connected to springs and dashpots. However, it can be treated as a free boundary here because the effects of the springs and dashpots are included in the form of external virtual work. In Sec. 7, the geometrical boundary condition on the pile head are a little different due to the presence of the anvil, which will be discussed further later.

$$\int_{t_0}^{t_1} \sum_{i=1}^{I} (\delta T_i - \delta U_i + \delta W_i)\,\mathrm{d}t + \int_{t_0}^{t_1} \sum_{i,i+1} \delta \Pi_{\lambda\kappa}\,\mathrm{d}t = 0 \tag{1}$$

$$\delta W_i = \iint_{S_i} (f_{u_i}\delta u_i + f_{v_i}\delta v_i + f_{w_i}\delta w_i) R\mathrm{d}x\mathrm{d}\theta \tag{2}$$

$$T_i = \frac{1}{2}\iint_{S_i} \rho h (u_i^2 + v_i^2 + w_i^2) R\mathrm{d}x\mathrm{d}\theta \tag{3}$$

$$\begin{aligned} U_i = \frac{K}{2}\iint_{S_i} & \left[\left(\frac{\partial u_i}{\partial x}\right)^2 + \frac{2\mu}{R}\frac{\partial u_i}{\partial x}\left(\frac{\partial v_i}{\partial \theta} + w_i\right) + \frac{1}{R^2}\left(\frac{\partial v_i}{\partial \theta} + w_i\right)\right. \\ & \left. + \frac{1-\mu}{2}\left(\frac{\partial v_i}{\partial x} + \frac{1}{R}\frac{\partial u_i}{\partial \theta}\right)^2\right] R\mathrm{d}x\mathrm{d}\theta \\ + \frac{D}{2}\iint_{S_i} & \left[\left(\frac{\partial^2 w_i}{\partial x^2}\right)^2 - \frac{2\mu}{R^2}\frac{\partial^2 w_i}{\partial x^2}\left(\frac{\partial v_i}{\partial \theta} - \frac{\partial^2 w_i}{\partial \theta^2}\right) + \frac{1}{R^4}\left(\frac{\partial v_i}{\partial \theta} - \frac{\partial^2 w_i}{\partial \theta^2}\right)^2\right. \\ & \left. + \frac{1-\mu}{2R^2}\left(\frac{\partial v_i}{\partial x} - 2\frac{\partial^2 w_i}{\partial x \partial \theta}\right)^2\right] R\mathrm{d}x\mathrm{d}\theta \end{aligned} \tag{4}$$

3.2. Admissible displacement functions

The displacement components u_i, v_i, w_i can be expanded in terms of admissible displacement functions weighted by generalized coordinates. Due to the incorporation of the interface potentials, the admissible displacement functions of each shell segment are not constrained to satisfy any continuity conditions or geometrical boundary conditions. They are only required to be linearly independent, complete and differentiable, which creates considerable flexibility in the selection of displacement functions. Compared with the analytical method, the effort to seek the in-vacuo natural modes is avoided, which significantly simplifies the solution process.

Good convergence has been observed when following four kinds of functions are adopted as axial displacement functions [26]: (a) Chebyshev orthogonal polynomials of the first kind; (b) Chebyshev

orthogonal polynomials of the second kind; (c) Legendre orthogonal polynomials of the first kind; (d) Hermite orthogonal polynomials [27]. In this model, Fourier series and Chebyshev orthogonal polynomials of the first kind are employed to expand the displacement variables in circumferential and axial directions, respectively. The displacement components of each sub-shell can be given as equation (5)~(7). $T_m(x)$ is the m^{th} order Chebyshev polynomial. M is the highest order Chebyshev polynomial taken in the computation. $\boldsymbol{U}(\bar{x},\theta), \boldsymbol{V}(\bar{x},\theta)$ and $\boldsymbol{W}(\bar{x},\theta)$ are the displacement function vectors in the three directions. $\boldsymbol{u}_i(\omega), \boldsymbol{v}_i(\omega)$ and $\boldsymbol{w}_i(\omega)$ are corresponding generalized coordinate vectors, with ω being the radian frequency and j being the imaginary unit. It should be noted that the Chebyshev polynomials are complete and orthogonal series defined on $\bar{x} \in [-1,1]$ interval while the actual axial coordinate in each sub-shell is defined on $x \in [0, l]$. Therefore, the coordinate transformations in equation (8) are introduced.

$$u_i(x,\theta,t) = \sum_{\alpha=0}^{1}\sum_{m=0}^{M}\sum_{n=0}^{\infty} T_m(\bar{x})\cos\left(n\theta + \alpha\frac{\pi}{2}\right)\bar{u}_{mn\alpha}(t) = \boldsymbol{U}(\bar{x},\theta)\boldsymbol{u}_i(\omega)e^{j\omega t} \tag{5}$$

$$v_i(x,\theta,t) = \sum_{\alpha=0}^{i}\sum_{m=0}^{M}\sum_{n=0}^{\infty} T_m(\bar{x})\sin\left(n\theta + \alpha\frac{\pi}{2}\right)\bar{v}_{mn\alpha}(t) = \boldsymbol{V}(\bar{x},\theta)\boldsymbol{v}_i(\omega)e^{j\omega t} \tag{6}$$

$$w_i(x,\theta,t) = \sum_{\alpha=0}^{1}\sum_{m=0}^{M}\sum_{n=0}^{\infty} T_m(\bar{x})\cos\left(n\theta + \alpha\frac{\pi}{2}\right)\bar{w}_{mn\alpha}(t) = \boldsymbol{W}(\bar{x},\theta)\boldsymbol{w}_i(\boldsymbol{\omega})e^{j\omega t} \tag{7}$$

$$x = \frac{l}{2}(\bar{x}+1), \quad \bar{x} = \frac{2}{l}x - 1 \tag{8}$$

3.3. The virtual work of fluid

Based on the assumptions given in Sec. 2, the motion of the fluid in frequency domain is described by the velocity potential $\emptyset(x,\theta,r,\omega)$ which satisfies Eq. (9). The fluid pressure in a circular cylindrical coordinate system, with certain regular boundary conditions, can be expanded as the summation of a set of analytical functions by applying variable separation technique. Each analytical function is considered as a pressure mode. The fluid-air interface is assumed to be a pressure released boundary and the seabed is considered as either a perfectly rigid boundary or a local impedance boundary. For the fluid field outside the pile, the fluid pressure and the velocity component normal to the surface of the shell can be given as Eq. (10) [23] and Eq. (11) [23].

$$\nabla^2\emptyset(x,\theta,r,\omega) + \left(\frac{\omega}{c}\right)^2\emptyset(x,\theta,r,\omega) = 0 \tag{9}$$

$$\tilde{p}_e(x,r,\theta) = -j\omega\rho_f\sum_{\alpha=0}^{1}\sum_{n=0}^{\infty}\sum_{p=0}^{\infty} D_{\alpha np}H_n^{(2)}(k_{rp}r)\sin k_{xp}(x-x_{es})\cos(n\theta+\alpha\frac{\pi}{2}) \tag{10}$$

$$\tilde{v}_{er}(x,r,\theta) = \sum_{\alpha=0}^{1}\sum_{n=0}^{\infty}\sum_{p=0}^{\infty} D_{\alpha np}H_n^{\prime(2)}(k_{rp}r)\sin k_{xp}(x-x_{es})\cos(n\theta+\alpha\frac{\pi}{2}) \tag{11}$$

In Eqs. (10) and (11), ρ_f is the density of the fluid. $H_n^{(2)}$ is the Hankel function of the second kind of order n and $H_n'^{(2)}$ denotes its derivative with respect to r.$D_{\alpha np}$ are unknown coefficients which are dependent on the radial displacements of the shell segments in contact with the fluid.

The terms k_{xp} and k_{rp} are wave numbers in x direction and r direction respectively and depend on radian frequency ω and boundary conditions on the sea surface and the seabed. The values of k_{xp} can be obtained according to Eq. (12), in which $p = 0, 1, 2, \cdots, \infty$, and $\tilde{Z}_{\text{soil}}(\omega)$ is the acoustic impedance of the seabed and can be measured with standard acoustic techniques [28]. It is obvious that k_{xp} are real values when the seabed is assumed to be perfectly rigid and complex values when the seabed is assumed to be an acoustic impedance boundary. $k_{rp} = \sqrt{(\omega/c)^2 - k_{xp}^2}$ are the wave numbers in radial direction and must satisfy the condition that $\text{Re}(k_{rp}) \geq 0$ and $\text{Im}(k_{rp}) \leq 0$ due to the requirement of radiation condition at $r \to \infty$.

$$\begin{aligned} k_{xp} &= \frac{(2p+1)\pi}{2(x_b - x_{es})}, && \text{(Rigid seabed)} \\ tan\, k_{xp}(x_b - x_{es}) &+ k_{xp}\frac{\tilde{Z}_{\text{soil}}(\omega)}{j\omega\rho_f} = 0 && \text{(Impedance seabed)} \end{aligned} \tag{12}$$

By making use of the normal velocity continuity condition on the fluid-structure interface and the orthogonality property of pressure modes, the unknown coefficient D_{np} can be obtained. Then the sound pressure in the exterior fluid field can be expressed as the summation of a set of analytical functions weighted by the radial displacement coordinates of the shell, i.e. $w_{i\alpha mn}$, as shown in Eq. (13).

$$\tilde{p}_e(x, r, \theta, \omega) = \sum_{i=1}^{I_e}\sum_{\alpha=0}^{1}\sum_{m=0}^{M}\sum_{n=0}^{\infty}\sum_{p=0}^{\infty} w_{i\alpha mn} \cdot \tilde{P}_{e,i\alpha mnp} \quad \text{with:}$$

$$\begin{aligned} \tilde{P}_{e,i\alpha mnp} = \frac{\omega^2\rho}{f_p}\frac{H_n^{(2)}(k_{rp}r)}{H_n'^{(2)}(k_{rp}R)} &\cdot \sin k_{xp}(x - x_{es}) \cdot \cos(n\theta + \alpha\frac{\pi}{2}) \\ &\cdot \int_{x_i}^{x_{i+1}} T_m(x - x_i) \cdot \sin k_{xp}(x - x_{es})\, dx \end{aligned} \tag{13}$$

and

$$f_p = \begin{cases} \dfrac{x_b - x_{es}}{2} & \text{(rigid seabed)} \\ \dfrac{x_b - x_{es}}{2} - \dfrac{1}{4k_{xp}}\sin 2k_{xp}(x_b - x_{es}) & \text{(impedance seabed)} \end{cases}$$

The effect of the fluid is considered as fluid loading acting on the pile. The virtual work done by the sound pressure on the shell is given as Eq. (14), with $\tilde{p}_e(x, R, \theta, \omega)$ being the sound pressure on the exterior surface of the shell and δw denoting the virtual displacement of the shell in radial direction. The derivation procedure of the virtual work of the interior fluid is completely analogous as that of exterior fluid pressure.

$$\delta W_p = \int_0^{2\pi}\int_{x_s}^{x_b} -\text{Re}(\tilde{p}_e(x, R, \theta, \omega)e^{j\omega t}) \cdot \delta w R \text{d}x\, \text{d}\theta \tag{14}$$

3.4. The virtual work of soil

A complete and absolutely exact evaluation of the influence of soil on the vibration and sound radiation of the pile is not easy to realize because the interactions between pile and its surrounding soil are very complex. In this work, the soil effect is incorporated into the model in a simple manner, in which the soil is modelled as uniformly distributed elastic springs and dashpots in all directions, as shown in Fig. 1. The effect of springs and dashpots on the pile shell is taken into consideration by incorporating their virtual work into the variation equation. The virtual works done by the springs and dashpots are given as equations (15) and (16), respectively. The spring coefficients and radiation damping are introduced to the model in a simple manner presented by Gazetas and Dobry [29]. The derivation of the radiation damping is based on the simplification treatment that the circular pile cross section is replaced by a square section having the same perimeter. It is further assumed that each of the four sides of the square emits only in the associated truncated quarter-plane and each of the four quarter-planes vibrates independently of the three others. Additionally, it is assumed that there is no tangential slip on the pile-soil interface. For detailed derivation of the radiation damping, the reader is referred to [29]. The derivation process of the spring coefficients is completely analogous as that of the radiation damping. The material damping of the soil is expressed with reference to an equivalent damping ratio of the soil throughout the frequency range for a certain strain rate [30]. The detailed expressions of the spring and damping coefficients are given in Appendix A.

The introduction of springs and dashpots is of practical significance from an engineering point of view, but it presents a challenge in the realistic evaluation of the coefficients and creates uncertainty to the calculations. The influence of the chosen spring and dashpot coefficients on sound radiation was discussed in the previous work [23] in which the similar simplification treatment was used. A complete modelling of the soil effect should take a variety of factors into consideration, such as the wave propagation in the soil field, the inhomogeneity and material nonlinearity of the soil, slippage and separation behaviour of the pile-soil interface, etc., which requires theoretical and experimental supports. This would be a significant research topic to follow by the authors and readers.

$$\delta W_{\mathrm{spring},i} = -\int_S (\delta u_i \cdot k_x u_i + \delta v_i \cdot k_\theta v_i + \delta w_i \cdot k_r w_i)\mathrm{d}s \tag{15}$$

$$\delta W_{\mathrm{dashpot},i} = -\int_S \left(\delta u_i \cdot c_x \frac{\partial u_i}{\partial t} + \delta v_i \cdot c_\theta \frac{\partial v_i}{\partial t} + \delta w_i \cdot c_r \frac{\partial w_i}{\partial t}\right)\mathrm{d}s \tag{16}$$

3.5. Impact force of the hammer

A practical and accurate evaluation of the impact force is of great importance for the prediction of the underwater noise because the force contains all the input energy of the interaction system. Analytic models [31, 32] were used to predict the pile-driving force for piles which transmit longitudinal wave. In these models the pile is simplified as a dashpot with constant impedance. For tubular piles the wave propagates along the pile with dispersion and the prediction of the impact force becomes more complicated. Reinhall and Dahl [16] got the approximate impact force as a step-exponential function by using the Finite Element (FE) impact analysis with the effect of the cushion, water and sediment neglected. Zampolli, et al. [15] adopted the similar function and obtained the peak force and decay time constant of the function by fitting the step-exponential pulse with the forcing curve obtained from a publicly available tool known as IHCWave [33]. Tsouvalas and Metrikine [23] used an impact force taken from a real case as the input of the interaction system. The amplitude and

wave form of the exciting force of the hydraulic hammer can be influenced by many factors, such as the categories of the impact pile drivers [34], the properties of the anvil and cushion, the size of the pile and the precise boundary condition on the pile top. Systematic investigations and further discussions are needed for the evaluation of impact forces in different situations.

In this work, the impact force is a fictitious one and it is assumed to distribute on the intersecting line of the neutral layer of the shell and the cross section on the pile top and is defined as Eq. (17). $F_0(\theta)$ is the distributed force dependent on θ and its unit is N m^{-1}. $H(t)$ is the waveform function in terms of time and its peak value is 1.

$$F(t) = H(t)\int_0^{2\pi} F_0(\theta) R \mathrm{d}\theta \tag{17}$$

3.6. Governing equations of the motion of the pile

In this work, the derivation of the equations is implemented in frequency domain. Therefore, Fourier transform pairs with respect to time and frequency [27] are introduced herein to transform variables between time domain and frequency domain. By performing the variation operation to Eq. (1) with respect to the generalized coordinate vectors $\boldsymbol{u}$, $\boldsymbol{v}$, $\boldsymbol{w}$ and substituting the virtual works of the hydraulic impact force, fluid pressure, spring and dashpot forces into the equation, the linear governing equations of the motion of the pile can be obtained as Eq. (18).

$$[-\omega^2\boldsymbol{M} + (\boldsymbol{K} - \boldsymbol{K}_\lambda + \boldsymbol{K}_\kappa) - \boldsymbol{C}_e + \boldsymbol{C}_i + j\omega\boldsymbol{C}_{\mathrm{soil}}]\boldsymbol{q}(\omega) = \boldsymbol{F}(\omega) \tag{18}$$

In the equation, $\boldsymbol{M}$ and $\boldsymbol{K}$ are the disjoint mass matrix and stiffness matrix of the shell, respectively. $\boldsymbol{K}_\lambda$ and $\boldsymbol{K}_\kappa$ are the generalized interface stiffness matrices incorporated by the Lagrange multipliers and interface least-squares weighted residual method, respectively [25]. The expressions of the matrices $\boldsymbol{M}$, $\boldsymbol{K}$, K_λ, K_κ and generalized force vector $\boldsymbol{F}(\omega)$ are given in the Appendix B. Matrices $\boldsymbol{C}_e$, $\boldsymbol{C}_i$ and $\boldsymbol{C}_{\mathrm{soil}}$ are coupling matrices introduced by the exterior sound pressure, the interior sound pressure and the soil in contact with the pile, respectively. The details of the matrices $\boldsymbol{C}_e$, $\boldsymbol{C}_i$ and $\boldsymbol{C}_{\mathrm{soil}}$ are given in Appendix C. The vector $\boldsymbol{q}(\omega)$ is the generalized coordinate vector consisting of the displacement coordinate vectors of the shell segments and its expression is given in Eq. (19). The sound radiation of the pile can be obtained by summing the pressure modes which are weighted by the radial generalized displacement coordinates.

$$\boldsymbol{q}(\omega) = \left[\boldsymbol{u}_1^{\mathrm{T}}, \boldsymbol{v}_1^{\mathrm{T}}, \boldsymbol{w}_1^{\mathrm{T}}, \boldsymbol{u}_2^{\mathrm{T}}, \boldsymbol{v}_2^{\mathrm{T}}, \boldsymbol{w}_2^{\mathrm{T}}, \cdots, \boldsymbol{u}_{\mathrm{I}}^{\mathrm{T}}, \boldsymbol{v}_{\mathrm{I}}^{\mathrm{T}}, \boldsymbol{w}_{\mathrm{I}}^{\mathrm{T}}\right]^{\mathrm{T}} \tag{19}$$

4. Dispersion relation and sound propagation characteristics

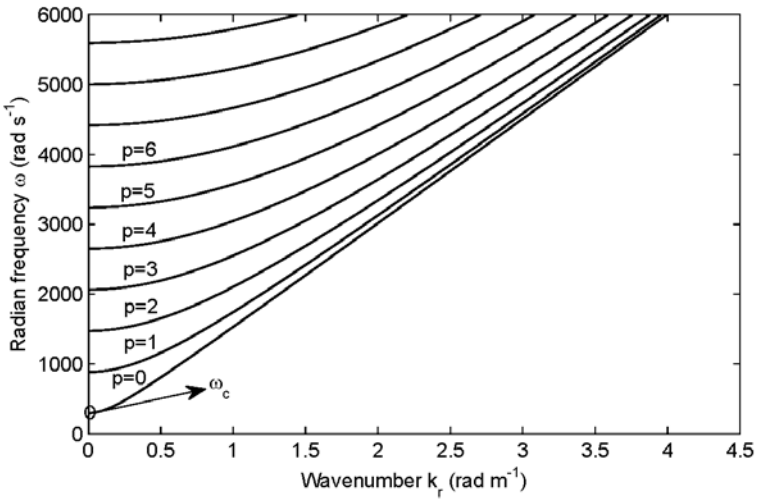

Fig. 3. Dispersion relation for rigid seabed

The analytical description of the sound pressure makes it possible to show the dispersion relation and examine the influence of some parameters on the sound radiation in a qualitative manner. As mentioned above, the wavenumbers in radial direction k_{rp} $(p = 0, 1, 2, \cdots)$ depend on the radian frequency and the wavenumbers in vertical direction k_{xp} which are dependent on the acoustic boundary condition on the seabed. In this section, the propagation characteristics of exterior sound radiation for the perfectly rigid seabed are discussed based on the dispersion relation ($\omega - k_r$ curves). The depth of the exterior seawater is assumed to be $x_b - x_{es} = 8$ m and the sound velocity is $c = 1500$ m s^{-1}.

For the rigid seabed, the wavenumbers in vertical direction are real and the wavenumbers in radial direction are either real (corresponding to propagating modes) or imaginary (corresponding to evanescent modes). The dispersion curves for the first ten pressure modes are shown in Fig. 3 for radian frequencies up to 6000 rad s^{-1}. As the radian frequency increases, the curvature of each curve decreases gradually and the phase velocity approaches to the defined sound velocity 1500 m s^{-1}. Each mode has a crossing point with the frequency axis which divides the frequency axis into a low frequency range and a high frequency range. In the low frequency range, radial wavenumber k_r is imaginary and the mode is evanescent. In the high frequency range, the wavenumber is real and the mode works as a propagating mode. Therefore, a cut-off frequency ω_c for propagating modes can be found at the crossing point of the frequency axis and the curve of the first pressure mode (corresponding to $p = 0$). Below the cut-off frequency, all modes become evanescent and no sound can propagate effectively away from the pile. By substituting the first equation of Eq. (12) into the expression $k_{rp} = \sqrt{(\omega_c/c)^2 - k_{xp}^2} = 0$, the cut-off frequency can be obtained as Eq. (20). It is obvious that the cut-off frequency is inversely proportional to the depth of the exterior fluid, which means low-frequency pile-driving noise in shallow waters is harder to propagate away than that in deep waters.

For the impedance seabed, the wavenumbers in both vertical direction and radial direction are complex-valued and dependent on the impedance of the seabed. In this situation, a clear cut-off

frequency no longer exists. For a more detailed analysis of the influence of the seabed impedance on the sound propagation, the reader is referred to [23].

$$\omega_c = \frac{c \cdot \pi}{2(x_b - x_{is})} \tag{20}$$

5. The case with an axisymmetric impact force

A pile with a certain geometry and material parameters is chosen for the axisymmetric numerical case. The seabed is assumed to be a perfectly rigid acoustic boundary. The material properties of the shell, geometry and parameters of the model are summarized in Table 1. The impact force is assumed to be axisymmetric and uniformly distributed on the circumference of the pile top. For this case displacement functions and pressure modes for only circumferential order $n = 0$ can be excited and the responses of the model are also axisymmetric. The distributed force is independent of angle θ, given as $F_0(\theta) = 1 \times 10^6$ N m^{-1}.The time function of the force is assumed to be a half sinusoid wave with a very small duration $\tau = 2.5$ ms and is given in Eq. (21).

$$H(t) = \begin{cases} \sin(\pi t/\tau) & 0 < t < \tau \\ 0 & t < 0 \text{ or } t > \tau \end{cases} \tag{21}$$

5.1. Truncation of the pressure modes and the number of sub-shells

Table 1. Model parameters (reference values) for the examined case

Parameters	Value	Unit
E	2.1×10^{11}	N m^{-2}
μ	0.28	–
ρ_s	7800	kg m^{-3}
η	0.002	–
L	28	m
R	1	m
h	0.02	m
c	1500	m s^{-1}
ρ_f	1000	kg m^{-3}
x_{es}=x_{is}	10	m
x_b	18	m
E_{soil}	5.0×10^7	N m^{-2}
μ_{soil}	0.4	–
ρ_{soil}	1600	kg m^{-3}

In the analytical expression, the sound pressure equals the summation of unlimited number of pressure modes consisting of both propagating modes and evanescent modes. It is important to include the evanescent modes in the solution scheme of the fluid-pile-soil interaction problem, especially for low frequencies. For each excitation frequency, there are a set of radial wavenumbers

$k_{rp} = 0, 1, 2, \cdots, \infty$ in the pressure expression, each of which corresponds to a pressure mode. Therefore, it is inevitable to truncate the modes in the computational program. As mentioned in Sec. 3.3, the wavenumbers in radial direction must satisfy the condition $\mathrm{Re}(k_{rp}) \geq 0$ and $\mathrm{Im}(k_{rp}) \leq 0$ because of the requirement of radiation condition at $r \to \infty$. It is noticed that evanescent modes are dramatically damped due to $e^{\mathrm{Im}(k_{rp})\cdot r}$ term. Therefore, only the modes with $e^{\mathrm{Im}(k_{rp})\cdot R} \geq \varepsilon$ are retained, with R being the radius of the pile and ε denoting a small parameter ($\varepsilon = 1 \times 10^{-4}$). The modes with $e^{\mathrm{Im}(k_{rp})\cdot R} < \varepsilon$ are disregarded because the contribution of the modes is negligible and the truncation leads to insignificant loss of accuracy.

Due to the accuracy requirement of high-frequency computation, the pile should be decomposed into enough number of shell segments with enough orders of admissible displacement functions adopted in each. Theoretically, increase of both the number of shell segments and the terms of the displacement functions can improve the accuracy of the model. However, excessively high orders of displacement functions should be avoided for two reasons. Firstly, there exists numerical integration of displacement functions in the variational equation and the integration of high orders of displacement functions is relatively inefficient. Secondly, incorporation of excessively high orders of displacement functions leads to badly conditioned structural mass matrixes and stiffness matrixes. Therefore, a better settlement for high-frequency computation is to increase the number of shell segments. The sound pressure responses of an observing position located 3 m above the seabed and 16 m away from the pile surface are calculated using different numbers of sub-shells, i.e. I =4, 6, 8, 10. A set of displacement functions with the highest order $M = 8$ is adopted in each sub-shell. The curves of the time histories are given in Fig. 4. Good convergence can be observed with such few sub-shells used. The curves of $I = 8$ and $I = 10$ are almost overlapped completely, which indicates a decomposition of 10 sub-shells would be accurate enough to predict the sound response of this case. In subsequent computation, the pile is decomposed into 12 sub-shells with 8 displacement functions in each. Further discussions about Fig. 4 are given in Sec. 5.3.

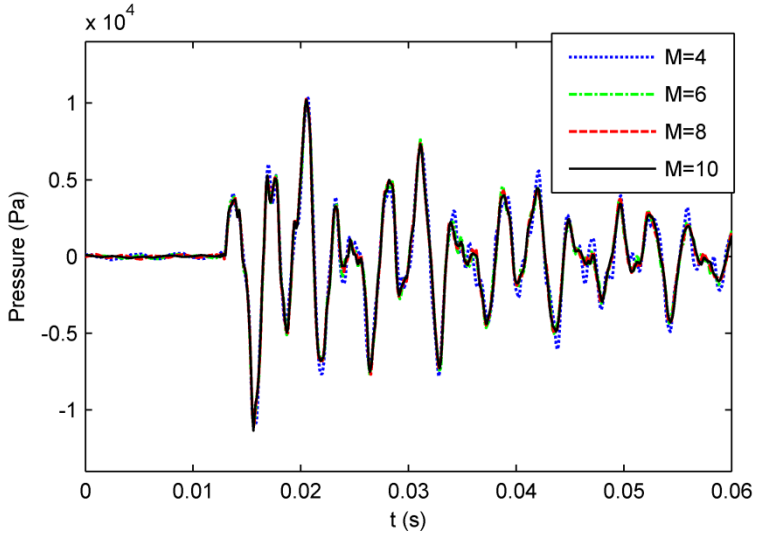

Fig. 4. Pressure histories at the observing position for different numbers of sub-shells

5.2. *Acoustic responses*

$$T_p(x,r,\omega) = \frac{p(x,r,\omega)}{F(\omega)} \tag{22}$$

$$f_{\text{ring}} = \frac{1}{2\pi R}\sqrt{\frac{E}{\rho_s(1-\mu^2)}} \tag{23}$$

The force to pressure transfer functions, defined as Eq. (22), for three observed points located 4 m below the sea surface are shown in Fig. 5. The ordinate values in dB are given by $20\log(|T_p|/T_0)$, with the reference value T_0 being 1 $\mu Pa\ N^{-1}$. The distances from the pile surface to each observed point are 8 m, 25 m and 50 m, respectively. It is evident that the difference between the three curves is depedent on frequency. The transfer function of a nearer observed position is generally higher than that of a farther observed position. An obvious trough can be observed at the ring frequency of the pile ($f_{\text{ring}} = 860$ Hz), defined as Eq. (23). At the ring frequency, the quasi-longitudinal wavelength in the shell wall equals the shell circumference and an axisymmetric, $n = 0$, 'breathing' or 'hoop', resonance occurs [11]. It was shown that a trough at this frequency also appeared on the frequency spectra of the radial pile displacement [21].

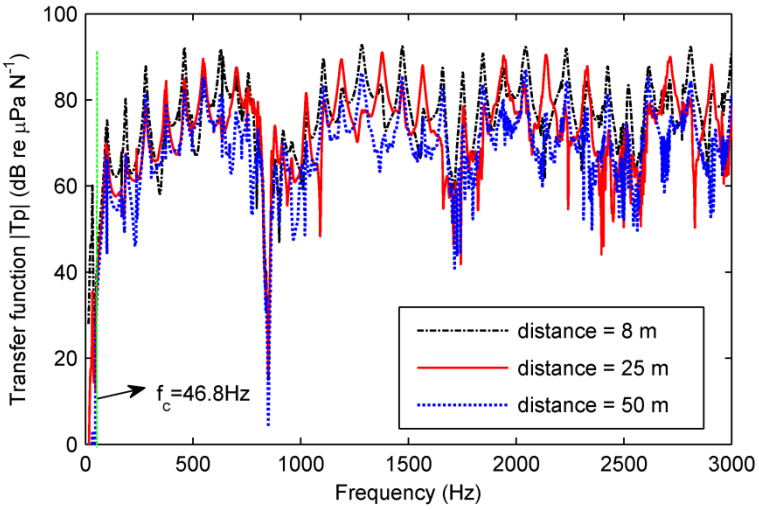

Fig. 5. Transfer functions for the observed points located 4 m below the sea surface

An obvious difference between the transfer functions is observed below the cut-off frequency $f_c =$ 46.8 Hz. In this frequency range the amplitutes are very small compared with those in the relatively high frequency range. This phenomenon can be ascribed to the fact that below the cut-off frequency there exist only evanescant modes which attenuate dramatically as radial distance increases. Below the cut-off frequency, the transfer function of the observed position at a distance of 50 m nearly vanishes and the curve climbs steeply at the cuf-off frequency.

The time histories of the pressures at the three points are given in Fig. 6. Increase in observed distance leads to both a lag along the time axis and an attentuation in amplitute. An estimated sound propagation speed from the figure is 1504 m s^{-1} which matches the defined sound speed $c = 1500$ m s^{-1} very precisely.

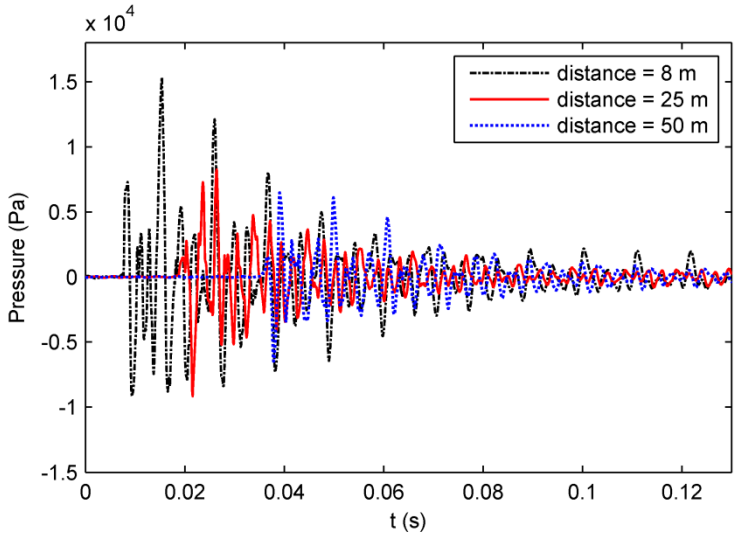

Fig. 6. Time histories of pressure for the observed points located 4 m below the sea surface

The force to pressure transfer functions for three observed points located 8 meters away from the pile surface are shown in Fig. 7. The points are positioned at 0.5 m, 4 m and 7.5 m below the sea surface, respectively. It is obvious that the sound pressure is depth dependent. Below 1400 Hz, The point close to the seabed has the highest peaks while the point close to the see surface has the lowest values. In the high frequency range, the trend no longer exists or even reverses. The pressure variation along depth depends on the terms $\sin k_{xp}(x - x_{es})$ in pressure modes, as given in equation (10). For each mode, a pressure trough emerges on the pressure release boundary and a pressure crest emerges on the rigid seabed. The aforementioned phenomenon in the low frequency range occurs because the upper point is close to the trough while the lower point is close to the crest. As the frequency increases, fluid modes of higher value of k_{xp} and smaller wavelengths become dominant. In high frequency range, the phenomenon no longer exists because the dominant wavelengths become comparable to or even smaller than the distance from the observed points to the adjacent boundaries.

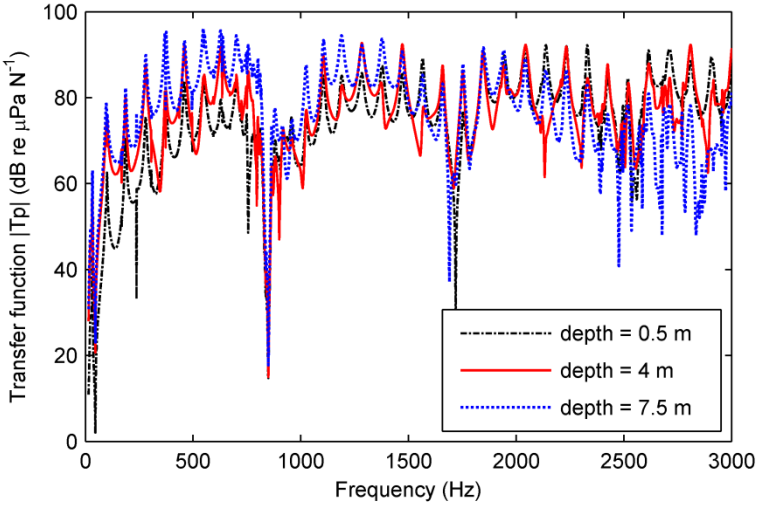

Fig. 7. Transfer functions for the observed points located 8 m away from the pile surface

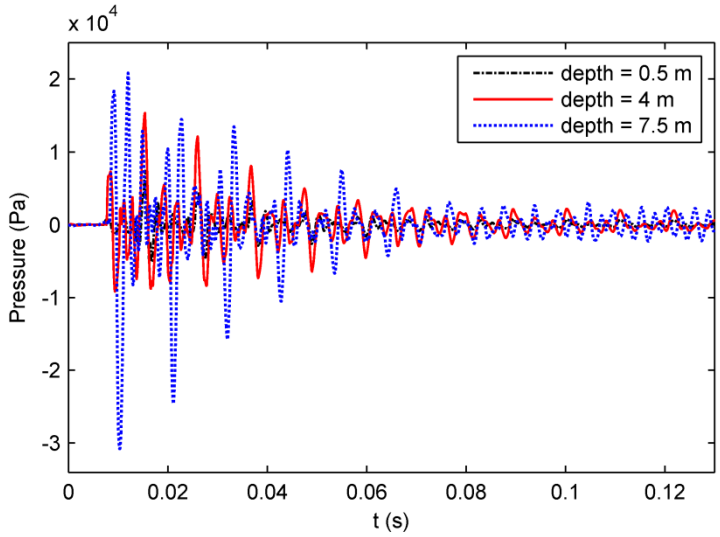

Fig. 8. Time histories of pressure for the observed points located 8 m away from the pile surface

Fig. 8 shows the time histories of the sound pressures at the three observed points. The pressure curves see their first peaks at about $t = 10$ ms and then fluctuate with a rapid attenuation along the time axis. The pressure amplitudes decrease to less than 5000 Pa after 70 ms. The point close to the seabed has the maximum pressure peaks while the point near the sea surface has the minimum values. This is based on the fact that in the low-frequency range the former observed point has the highest while the later one has the lowest pressure amplitude and most energy of the impact force is distributed in this frequency range. The absence of strong peaks at the depth of 0.5 m is discussed further in the Sec. 5.3.

5.3. Pressure distributions in exterior fluid field

In Fig. 9, the pressure level distributions on a cross section of the fluid field are shown for 4 different frequencies. The values are presented in terms of sound pressure levels (SPL) calculated by Eq. (24), with the reference value being $\tilde{p}_0 = 1\,\mu Pa/\mathrm{Hz}$. The horizontal axis shows the radial distance from the pile surface and the vertical axis denotes the depth of the exterior fluid measured from the sea surface. As mentioned above, the pressure variation along depth depends on the terms $\sin k_{xp}(x - x_{es})$ in pressure modes, with k_{xp} given in Eq. (12). For each mode, the pressure vanishes on the surface and reaches its wave crest on the seabed. From the Fig. 9 (a), it is observed that the mode corresponding to $p = 0$ seems to be dominant over other modes. This can be explained by the dispersion curves given in Fig. 3. For this frequency $\omega = 2\pi f = 314$ rad s^{-1}, only the mode corresponding to $p = 0$ contributes as a propagating mode and all the other modes are evanescent. As for the Fig. 9 (b) whose radian frequency is 1256 rad s^{-1}, there are two propagating modes contributing to the sound pressure, i.e. p =0 and p =1. A nodal line tends to emerge at the depth of 5.3 m, which indicates that the later mode is predominant over the former one. When the frequency increases, there will be more propagating modes involved and their relative contributions to the pressure field are dependent on the structural deformation of the shell. It can be seen from the other two figures that the dominant modes for 1000 Hz and 2000 Hz are corresponding to p =2 and p =5, respectively. For all the four figures, the sound pressure levels attenuate as the radial distance increases. Due to the presence of evanescent modes which are only significant near the pile surface, the attenuations of the pressure levels are especially noticeable at the proximity of the shell surface.

$$\mathrm{SPL} = 20\log_{10}\left(\frac{\sqrt{2}}{2}\frac{|\tilde{p}_e(x,r,\theta,\omega)|}{\tilde{p}_0}\right) \tag{24}$$

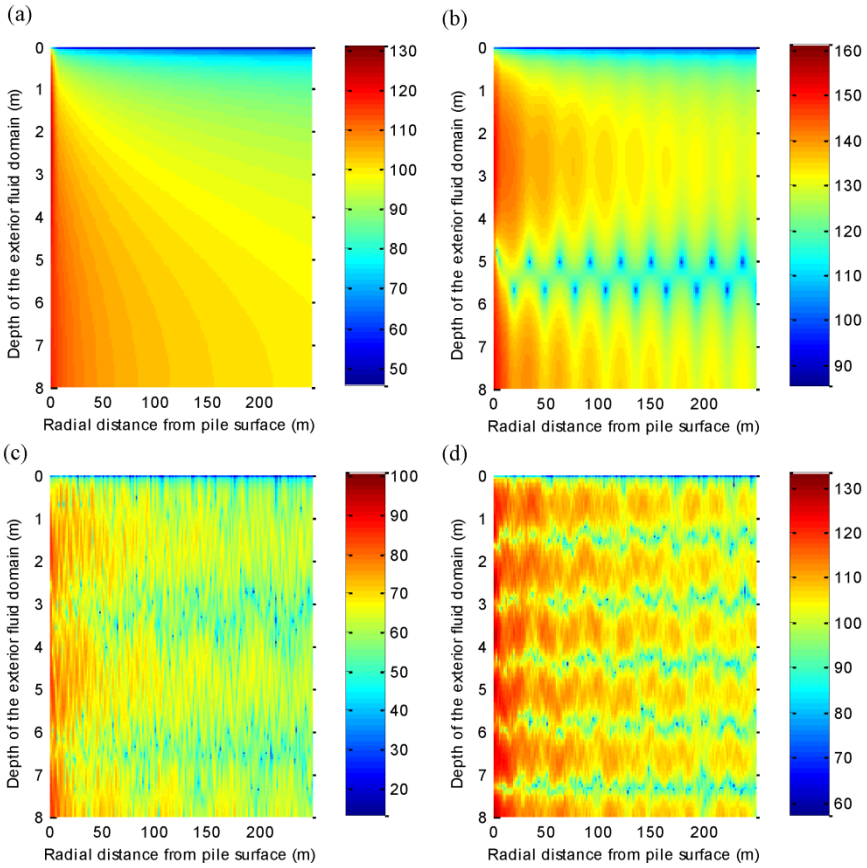

Fig. 9. Distributions of pressure level in dB re 1 μPa/Hz for

(a) 50 Hz, (b) 200 Hz, (c) 1000 Hz and (d) 2000 Hz

The evolution of the radiated exterior pressure with time for a radial distance up to 16 m is illustrated in Fig. 10. The time step between two adjacent pictures is 2 ms. A compressional wave is excited by the impact force at the pile top and propagates rapidly downwards. When the structural wave goes through the fluid field, the fluid is compressed and generates a pressure peak which propagates outward along the radial direction. A minus pressure peak is generated immediately after the positive pressure peak due to the rarefaction following after the compression. The structural wave in the pile propagates faster than the sound velocity of the fluid, therefore a Mach cone [14, 16] is formed in the fluid field with an angle α with respect to the pile axis. The angle depends on the relation $\alpha = \tan^{-1}(c/c_s)$ in which c_s is the propagation speed of the structural wave in the pile. An estimated value of the angle from the figure is 16.5°. The approximate propagation speed of structural wave is 5064 m s^{-1} which is slightly smaller than longitudinal wave velocity in the steel material $c_L = \sqrt{E/\rho_s} = 5188$ m s^{-1}. This presence of Mach cones was initially mentioned in [14] and was also observed in [16, 17, 23]. For a detailed description of the structural wave velocity and its dispersion characteristics in the pile wall, the reader is referred to [21, 22]. When the compressed structural wave arrives at the pile bottom it is reflected backward due to the impedance difference on the pile end. The upward reflected wave compresses the fluid and again an upward Mach cone generates in the fluid.

The upward Mach cone can be observed in the last two pictures. It is worth noting that there is an area along the sea surface where the downward Mach cones cannot be seen. Reinhall and Dahl [16] pointed out that the depth of the area is $D^* \approx R \cdot \tan\alpha$, with R being the radial distance from the pile source and α being the angle of the Mach cone. The absence of downward Mach cones on this area leads to the lack of strong pressure peaks at points close to the sea surface, which gives further explanation on the phenomenon observed in Fig. 8. Away from the pile interface and for the points 0.5 m below the surface the powerful Mach cones are not present and strong pressure peaks cannot be found. However, if one moves very close to the pile-fluid interface, the pressure difference in vertical direction will no longer be so obvious due to the formation of the Mach cones.

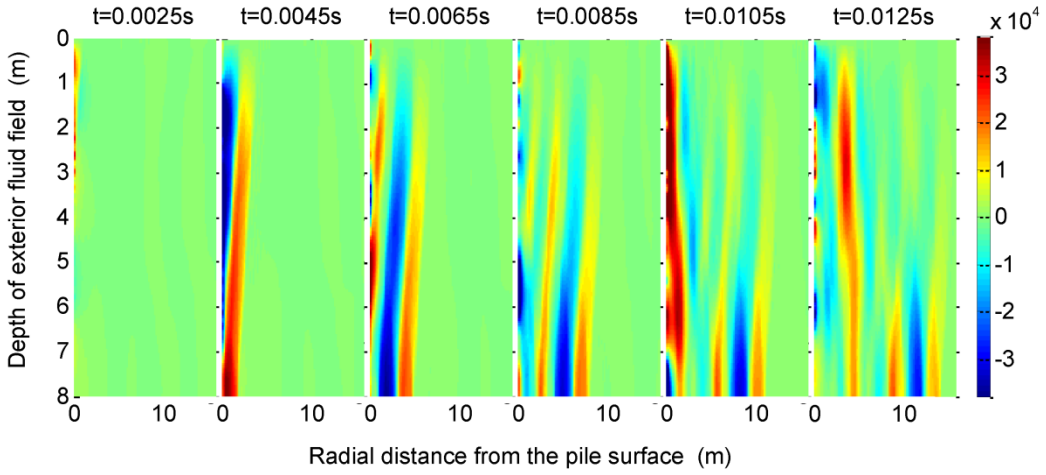

Fig. 10. Evolution of the sound pressure in Pa for time steps starting from 2.5 ms to 12.5 ms

It takes about 0.01 *s* for the structural wave to travel twice the length of the pile. We call this duration a quasi-periodicity. In every quasi-periodicity, the vibration energy of the pile decays significantly as a portion of it is transmited into water and comsumed on the pile-soil interface. As a result, the sound energy has a similar decaying trend. If we examine the curve in Fig. 4 by an interval of about 0.01s, we can observe the quasi-periodicity and find the pressure decay in each quasi-periodicity is very obvious.

5.4. The effect of varied impact force on the sound radiation

Deeks and Randolph [31] revealed that the amplitude and the duration of the pile-driving force was strongly influenced by the cushion stiffness, the anvil mass and the cushion damping. The variation of the impact force can make a significant difference to the pile driving noise. In this section, the effect of varied impact force on the sound responses is investigated.

A set of half sinusoid forces $F_i(t)$, as given in Eq. (25), are used as the inputs of the model, with F_0^i and τ_i being the peak distributed force and the duration of the force $F_i(t)$, respectively. They are assumed to impart equal impulse $I_F = \int F_i(t)\mathrm{d}t$ to the pile head and satisfy Eq. (26), with $F_0 = 1 \times 10^6\ Nm^{-1}$, $\tau_0 = 2.5$ ms. The evaluated durations τ_i increase from 1.25 ms to 5 ms, while the corresponding peak distributed forces F_0^i decrease from $2\mathrm{F}_0$ to $0.5\mathrm{F}_0$. The evaluated output quantities are the peak sound pressure level ($\mathrm{SPL}_{\mathrm{peak}}$) and the single sound exposure level (SEL), derived from the sound pressure p at the observed position 4 m below the sea surface and 40 m away from the pile surface. The output quantities are defined as Eq. (27) and Eq. (28), with the reference pressure and

time being $p_0 = 1\,\mu Pa$ and $t_0 = 1\,s$, respectively. The sound response of interest is within the interval between t_1 and t_2.

The SPL_{peak} and SEL curves for the forces are given in Fig. 11. Both curves experience a significant decline as the force duration increases. Four times of decrease in force peak (from $2F_0$ to $0.5F_0$) leads to a decline of SPL_{peak} and SEL as much as 20 dB, which means the peak pressure decreases 10 times. The fact that the change in sound pressure is more significant than the change in the force peaks would be explained by evaluating the structural wave excited by the hammer force. In addition to the force peak, the force duration make a significant impact on the structural wave. At the very moment when the hammer bounce away from the pile top, the structural deformation covers a length of $c_s\tau_i$ on the pile, which indicates that, for a short force duration τ_i, the structural deformation covers less length and the radial displacement varies more sharp in axial direction. It means that a more powerful structural wave would generate, transmit on the pile, and radiate higher level of underwater sound. The results suggest that it would be a potential way to reduce pile driving noise by choosing appropriate anvil and cushion.

$$F_i(t) = \begin{cases} 2\pi R F_0^i \sin\left(\dfrac{\pi t}{\tau_i}\right) & 0 < t < \tau \\ 0 & t < 0 \text{ or } t > \tau \end{cases}, \quad (i = 1, 2, \cdots, 21) \tag{25}$$

$$\int_0^{\tau_i} 2\pi R F_0^i \sin(\pi t/\tau_i)\,\mathrm{d}t = \int_0^{\tau_0} 2\pi R F_0 \sin(\pi t/\tau_0)\,\mathrm{d}t \tag{26}$$

$$\mathrm{SPL}_{peak} = 20\log_{10}\left(\frac{\max[abs(p)]}{p_0}\right) \tag{27}$$

$$\mathrm{SEL} = 10\log_{10}\left(\frac{1}{t_0}\int_{t_1}^{t_2}\frac{p^2}{p_0^2}\,\mathrm{d}t\right) \tag{28}$$

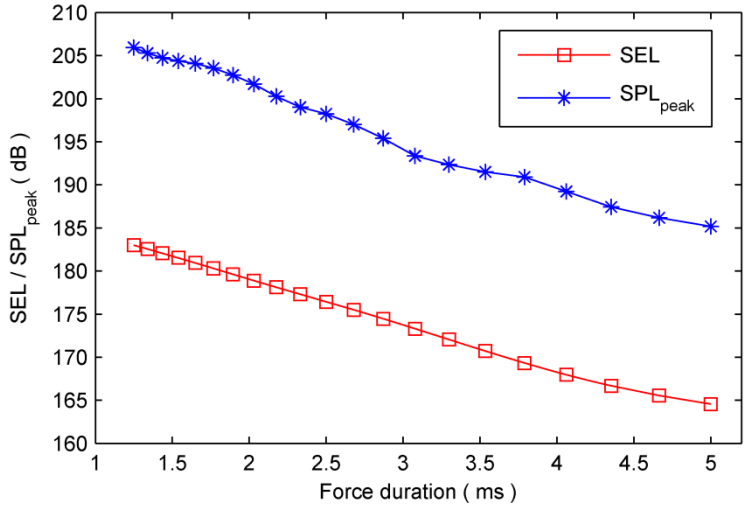

Fig. 11. SPL_{peak} (re 1 μPa) and SEL (re 1 $\mu Pa^2/s$) values for varied impact force.

6. The case with a non-axisymmetric impact force

In the previous case, the impact force is an ideal one which only excites axisymmetric vibration and sound radiation. In practice, it is difficult to keep the impact force absolutely parallel with pile axis and uniformly distributed on the circumference. In this section, a non-axisymmetric case whose impact force is dependent on circumferential angle is studied. The material and geometrical parameters are summarized in Table 1 and the impact force of the hammer is an assumed distributed force given in Fig. 12. The force can be considered as the summation of a uniformly distributed force $F_1 = 1 \times 10^6$ N m^{-1} and an angle-dependent distributed force. The time function $H(t)$ is the same with the previous case and is given in Eq. (21). Other than the axisymmetric case in which only the axisymmetric modes (corresponding to $n = 0$) are included in the program, a non-axisymmetric case must take the non-axisymmetric modes (corresponding to $n > 1$) into consideration. For the specified force given in Fig. 11, one only needs to include the modes with $n = 0$ and $n = 1$ into the program because the force doesn't excite pressure modes with higher circumferential orders.

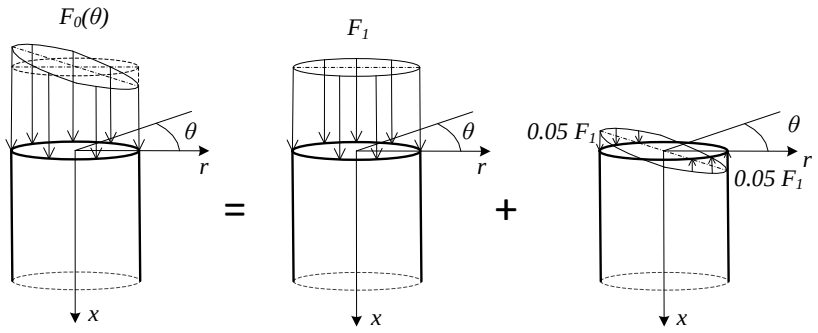

Fig. 12. Modeling of the non-axisymmetric impact force

In Fig. 13, the sound responses in frequency domain of four observed positions located 40 m away from the pile surface and 4 m below the sea surface are shown. The first 3 curves are spectrums of the points positioned at $\theta = 0$, $\pi/2$ rad and π rad, respectively. The last curve is the pressure response of the axisymmetric case in which only the axisymmetric distributed force F_1 is applied. In this non-axisymmetric case, the impact force as well as the acoustic response can be regarded as the summation of two components, i.e. the axisymmetric component and the non-axisymmetric component. Therefore, the difference in μPa s between each curve and the fourth curve equal the pressure response caused by the non-axisymmetric component. The axisymmetric response is completely overlapped with the pressure spectrum of the position located at $\theta = \pi/2$ rad, which means that the sound pressure caused by the non-axisymmetric component vanishes at this point. Theoretically, there exists a cross section plane ($\theta = \pi/2$ rad) in the exterior sound field on which the sound pressure caused by the non-axisymmetric component vanishes. This is based on the fact that the pressure modes corresponding to $n = 1$ contribute to the non-axisymmetric sound radiation and this section plane is on the nodal plane of the pressure modes.

The curves in Fig. 13 experience several evident troughs as the frequency increases. An analysis of the frequency spectrum of the impact force finds that its amplitude decreses as the frequency increases and vanishes at the frequencies $f_q = (1/2 + q)/\tau$, with the index being $q = 1, 2, 3, \cdots$. Therefore, the pressure spectrums of the observed points see a downward trend as the frequency arises and experience several sharp troughs. The first trough emerges at $f_1 = 600$ Hz and troughs appear again every 400 Hz along the frequency axis. For a specific shape of the impact force, a small duration of

the force will lead to a result that the main energy of the force distributes on a wide range. In other words, the faster the force attenuation is in time domain, the slower the spectrum attenuation is in frequency domain. The impact force used in the model determines how the energy is distributed in the frequency domain. Actually, the frequency spectrum of the sound pressure in the fluid field is atrongly influenced by the wave shape, amplitude and duration of the hammer force. Generally, the impact force of pile driving has a duration within several milliseconds, and the sound energy is mainly distributed on the low frequency range. As can be seen from Fig. 13, the SPL peaks over 2000 Hz are approximately 40 dB less than the peaks below 500 Hz. The impact forces in these two cases are hypothetical ones which create great convenience for the computation. However, as mentioned in Sec. 3.5, systematic studies and further discussions are necessary for more accurate and practical evaluations of the impact force with a variery of factors consided.

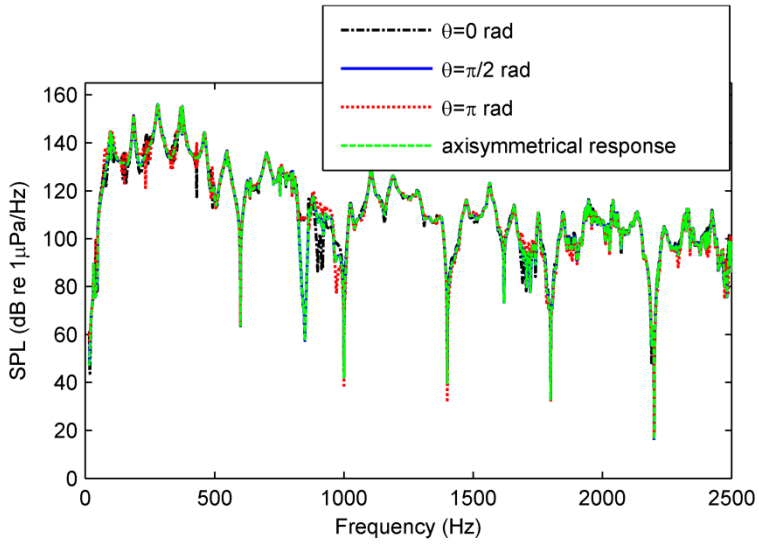

Fig. 13. Pressure levels of four observed positions distributed 4 m below the sea surface

Fig. 13 shows that the axisymmetric response has an obvious trough around the ring frequency ($f_{\mathrm{ring}} = 860$ Hz), which is consistent with the phenomenon observed in Fig. 5. However, the trough cannot be found from the non-axisymmetric responses at the observed points with $\theta = 0$ and $\theta = \pi/2$ rad. The comparison between the curves shows that the radiated sound is not uniformly distributed in circumferential direction for the entire frequency range and the circumferential non-uniformity is especially obvious around the ring frequency of the pile. It is clear that around the ring frequency only the responses of non-axisymmetric modes are significant. The difference between the curves indicates that experimental signal acquisition of underwater pile-driving noise in just one direction would not be enough, especially when the impact force has a significant non-axisymmetric component. The discovery of circumferential non-uniformity of the sound field is of guiding significance for the experimental tests of the underwater pile driving noise.

7. The case including the pile cap

On the one hand, the interaction between the ram, the cushion, the anvil and the pile influences the impact force [31, 35], and on the other hand their presence would influence the mechanical responses of the pile. In this section, a pile anvil seated on the pile head is included into the model, as illustrated in Fig. 14. Following assumptions are used to this model: a). the impact force is a vertical force

coaxial with the pile axis; b). the anvil is assumed as a lumped mass simply supported on the pile head, i.e., the anvil moves vertically together with the pile head without separation and the interface between the anvil and the pile head doesn't sustain shear forces and bending moments. The impact force is the same with the one used in Sec. 5.1~ Sec. 5.3.

The second assumption means that an additional axial inertia force is applied to the pile head as the anvil moves along with it. The effect of the anvil is taken into account by incorporating the kinetic energy of the anvil T_a into the variational equation (1). Then the variational equation turns to be Eq. (29), with T_c given in Eq. (30). u_0 is the displacement of the pile head in axial direction. By this approach, one only needs to change the mass matrix of the first sub-shell to get the new governing equations. The mass sub-matrix of this case is also given in Appendix B.

$$\int_{t_0}^{t_1}\left[\delta T_c + \sum_{i=1}^{I}(\delta T_i - \delta U_i + \delta W_i)\right]\mathrm{d}t + \int_{t_0}^{t_1}\sum_{i,i+1}\delta \Pi_{\lambda\kappa}\ \mathrm{d}t = 0 \tag{29}$$

$$T_c = \frac{1}{2}m_c u_0^2 \tag{30}$$

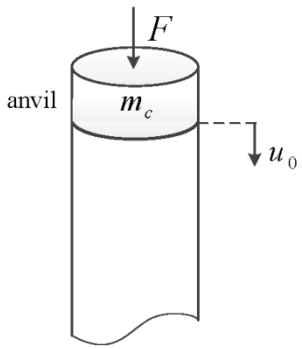

Fig. 14. The impact model of the anvil

In Fig. 15, the SPL curve of the case including an anvil ($m_c = 600$ kg) is compared with the case without the anvil at an observed position. It is shown that the anvil tends to reduce the corresponding frequencies of the peaks, which can be explained by the fact that the anvil introduces additional mass to the coupling system. Furthermore, the corresponding amplitudes of the peaks tend to decrease due to the presence of the anvil. Both the trends become more evident in the high-frequency range. The incorporation of the anvil changes the geometrical boundary condition on the pile top, and changes the resonance frequencies and the response amplitudes of the model. The change becomes increasingly sensitive to the variation of boundary condition as the frequency goes up. In this case, the incorporation of the anvil doesn't result in obvious losses in $\mathrm{SPL_{peak}}$ and SEL at the position, which are just 0.5 dB and 0.3 dB, respectively. It can be concluded that the losses in $\mathrm{SPL_{peak}}$ and SEL will be more significant if a sharper force impacts on the pile, since a sharper force carries more energy on the high frequency range.

The variational formulation makes it quite tractable to deal with piles with complex boundary conditions in which some attachments are connected to the pile ends, such as the pile cap (anvil), the pile cushion and the pile footing. Compared to the method using differential equations to solve the shell displacements, the effort to seek in-vacuo shell modes for different geometrical boundary conditions is avoided. This advantage makes it possible to establish a more complete model for

influence evaluation of the attachments and to explore potential noise-reducing measures, which would be a potential work for the authors and the readers.

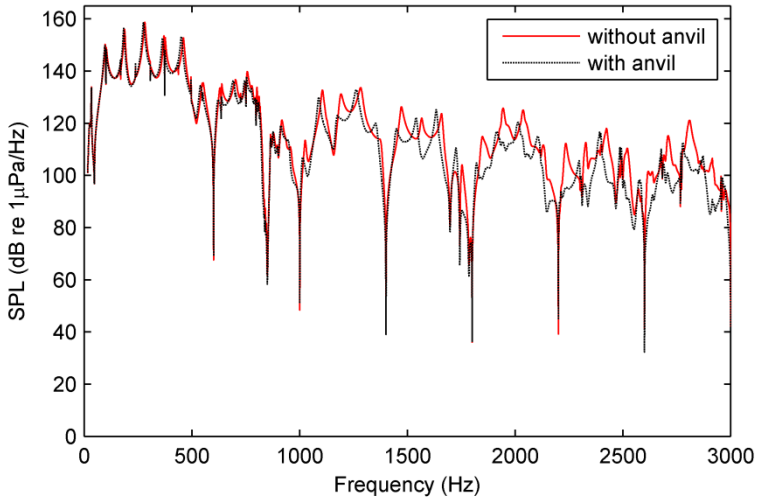

Fig. 15. Pressure levels at the point located 4 m below the sea surface and 10 m away from the pile surface.

8. Experimental validation

To validate the modeling approach described in Sec. 3, a comparison between measured data from the sound test of a mini pile and computed values from the mechanical model is given in this section. The experiment was conducted in a lake whose water depth was much less than that of an offshore site and the size of the pile was also far lower than that of a real pile used in offshore pile driving. The data comparison presented in this work offers experiment support for the modeling approach, but both the measured data and the computed values cannot reveal the real characteristics of the offshore pile driving noise due to the huge size difference.

A pile with a length of 4.6 *m*, a diameter of 139 *mm* and a thickness of 2 *mm* was driven into the lake bottom. The length of the pile below the water-soil interface was about 0.4 *m*. The material parameters of the pile are listed in Tab. 1. The average water depth of the site was about 1.7 *m*. A disc-shaped pile cap with a mass of 2.5 *kg* was fixed on the pile top by a flange connection. A hammer, equipped with a force sensor, impacted on the geometrical center of the upper surface of the cap and the sound signal was collected by a hydrophone located at the position 3 *m* away from the pile surface and 0.65 *m* below the air-water surface. The impacts were repeated 5 times for average and the time interval between any two adjacent impacts was large enough for the sound signal excited by the former impact to vanish. The average peak force was 1817 *N* and the average duration of the force was 1.95 *ms*. The data were collected with a sampling frequency of 8192 Hz. The test of the ambient noise found it was negligible compared with collected pile driving noise. At the observed position, no significant reflected sound wave from the lake shore was detected during the time interval of interest.

The bottom of the site was characterized by a thin layer of soft clay with a thickness of approximately 0.8 m, overlying a relatively hard clay bottom. In the theoretical computation, the soil parameters were chose according to the upper layer of soil. A sample analysis of the upper layer suggested its density was about $\rho_{\mathrm{soil}} = 1720\ kg/m^3$. The soil's elastic modulus and the Poisson's

ratio used for theoretical computation were respectively $E_{\text{soil}} = 3.5\,MPa$ and $\mu_{\text{soil}} = 0.4$, which were chose according to the suggestion of the reference [36] for soft clay. In the theoretical model, the water-soil interface is assumed to be a rigid acoustic boundary, and the radial displacement w at the pile top is confined to be zero in consideration of the effect of the flange connection.

A comparison between the computed sound pressure and the measured sound pressure is given in Fig. 16, in which the measured data are the average output of the five impacts. The curves show that the model can reproduce the main characteristics of the response in both time domain (Fig. 16a) and frequency domain (Fig. 16b), albeit with some deviations on the pressure peaks and resonance frequencies. In the frequency range of interest, the resonance frequencies are not as dense as those presented in Fig. 5 and Fig. 7, which can be explained by the fact that the modal density of the mini pile is far lower than that of the previous one within this frequency range. The computed SPL_{peak} and SEL values are respectively 3.4 dB and 1.4 dB larger than their corresponding measured data. Both the soil simplification and the rigid assumption of acoustic bottom introduce accuracy loss to the model, and these errors are inevitable on this topic due to the complex composition of the model. Due to a number of uncertainties, prediction errors of underwater pile driving noise at these scales are common [19, 23], such as the parameter uncertainties of soil, the contact condition uncertainties at the pile-soil and anvil-pile interfaces, and the variations of the pile geometry. In addition to the overestimate of pressure peak, the theoretical model gives a higher evaluation to the pressure decay over time, which suggests that the spring and dashpot model would overrate the damping of the soil. The comparison to the experiment data indicates that the presented model is capable of predicting the underwater pile driving noise quantitatively in both time domain and frequency domain, albeit with some errors.

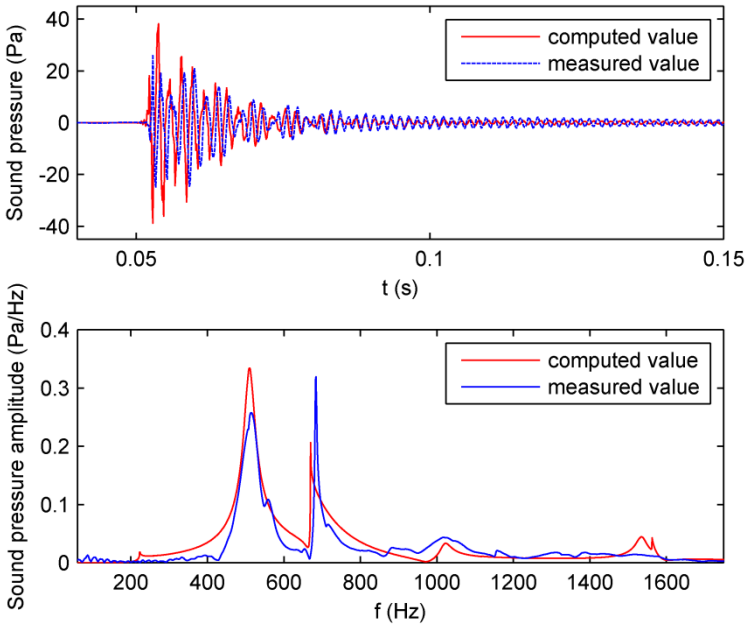

Fig. 16. Comparison of computed and measured sound pressures at the position located 3 m away from the pile surface and 0.65 m below the air-water interface in (a) time domain and (b) frequency domain.

9. Conclusions

In this work, a new semi-analytical methodology is proposed to establish the mechanical model for predicting the underwater noise for a pile-water-soil interaction system subject to piling hammer impacts. Based on the study, following conclusions can be obtained:

The dispersion relation curves show that for perfectly rigid seabed there is a cut-off frequency for sound propagation in the exterior fluid field. Underwater noise below the cut-off frequency cannot propagate effectively away from the pile. The value of the cut-off frequency is inversely proportional to the depth of the exterior fluid, which indicates that low-frequency pile-driving noise in shallow waters is harder to propagate away than that in deep waters. The sound outputs of a set of impact forces with equal impulse shows that both the SEL and the $\mathrm{SPL}_{\mathrm{peak}}$ decreases significantly as the force duration increases. The non-axisymmetric case indicates that the radiated sound pressure has dependence on circumferential angle, and around the ring frequency of the pile the sound pressure is mainly contributed by the non-axisymmetric pressure modes. The presence of the anvil tends to reduce the corresponding frequencies and amplitudes of the peaks of the sound pressure level, and this tendency becomes more obvious as the frequency increases. However, in the presented case the anvil doesn't influence the underwater SEL and the $\mathrm{SPL}_{\mathrm{peal}}$ significantly.

A mini pile experiment has demonstrated that the developed semi-analytical method is reliable to predict the pile driving noise in both time and frequency domains, albeit with some accuracy loss.

Acknowledgements

This work is supported by grant 11272208 of the National Science Foundation of China (NSFC). The authors gratefully acknowledge Dr. Haijun Wu from Shanghai Jiao Tong University for his valuable discussions and suggestions.

Appendix A. Expressions of the spring and damping coefficients

The equivalent spring coefficients for the soil model in three directions are given as

$$k_x = \rho V_s \omega \cdot \mathrm{Re}\left[\frac{H_1^{(2)}\left(\frac{\pi}{4}\frac{\omega R}{V_s}\right)}{H_0^{(2)}\left(\frac{\pi}{4}\frac{\omega R}{V_s}\right)}\right], \tag{A.1a-c}$$

$$k_r = \frac{1}{2}\rho\omega \cdot \mathrm{Re}\left[V_s \frac{H_1^{(2)}\left(\frac{\pi}{4}\frac{\omega R}{V_s}\right)}{H_0^{(2)}\left(\frac{\pi}{4}\frac{\omega R}{V_s}\right)} + V_{La}\frac{H_1^{(2)}\left(\frac{\pi}{4}\frac{\omega R}{V_{La}}\right)}{H_0^{(2)}\left(\frac{\pi}{4}\frac{\omega R}{V_{La}}\right)}\right],$$

$$k_\theta = \frac{1}{2}\rho V_s \omega \cdot \mathrm{Re}\left[\frac{H_1^{(2)}\left(\frac{\pi}{4}\frac{\omega R}{V_s}\right)}{H_0^{(2)}\left(\frac{\pi}{4}\frac{\omega R}{V_s}\right)}\right],$$

with $V_s = \sqrt{E_{soil}/[2(1+\mu_{soil})\rho_{soil}]}$ being the shear wave velocity of the soil and $V_{La} = 3.4V_s/[\pi(1-\mu_{soil})]$ denoting the *Lysmer's analog* wave velocity [29].

The equivalent damping coefficients in three directions are given as

$$c_x = \rho V_s \cdot \mathrm{Re}\left[-i\frac{H_1^{(2)}\left(\frac{\pi}{4}\frac{\omega R}{V_s}\right)}{H_0^{(2)}\left(\frac{\pi}{4}\frac{\omega R}{V_s}\right)}\right] + 2k_x\frac{\beta_{soil}}{\omega},$$

$$c_r = \frac{1}{2}\rho \cdot \mathrm{Re}\left[-i \cdot V_s\frac{H_1^{(2)}\left(\frac{\pi}{4}\frac{\omega R}{V_s}\right)}{H_0^{(2)}\left(\frac{\pi}{4}\frac{\omega R}{V_s}\right)} - i \cdot V_{La}\frac{H_1^{(2)}\left(\frac{\pi}{4}\frac{\omega R}{V_{La}}\right)}{H_0^{(2)}\left(\frac{\pi}{4}\frac{\omega R}{V_{La}}\right)}\right] + 2k_r\frac{\beta_{soil}}{\omega},$$

$$c_\theta = \frac{1}{2}\rho V_s \cdot \mathrm{Re}\left[-i\frac{H_1^{(2)}\left(\frac{\pi}{4}\frac{\omega R}{V_s}\right)}{H_0^{(2)}\left(\frac{\pi}{4}\frac{\omega R}{V_s}\right)}\right] + 2k_\theta\frac{\beta_{soil}}{\omega}. \quad \text{(A.2a-c)}$$

In each equation ,the first part in the right side is the radiation damping coefficient in corresponding direction [29], while the second part denotes corresponding material damping coefficient, with β_{soil} being the equivalent damping ratio depending on the level of soil strain [30], which can be evaluated roughly by examining the vibration responses of the soil-free model.

Appendix B. Expressions of $\boldsymbol{M}$, $\boldsymbol{K}$, $\mathbf{K}_{\boldsymbol{\lambda}}$, $\mathbf{K}_{\boldsymbol{\kappa}}$ and $\boldsymbol{F}(\boldsymbol{\omega})$

The disjoint mass and stiffness matrices $\boldsymbol{M}$, $\boldsymbol{K}$ are respectively given as

$$\boldsymbol{M} = \mathrm{diag}[\boldsymbol{M}_1, \boldsymbol{M}_2, \cdots, \boldsymbol{M}_i, \cdots, \boldsymbol{M}_I]; \quad \boldsymbol{K} = \mathrm{diag}[\boldsymbol{K}_1, \boldsymbol{K}_2, \cdots, \boldsymbol{K}_i, \cdots, \boldsymbol{K}_I] \quad \text{(B.1a-b)}$$

in which sub-matrices $\boldsymbol{M}_i$ and $\boldsymbol{K}_i$ are mass and stiffness matrices of the i^{th} sub-shell given as

$$\boldsymbol{M}_i = \begin{bmatrix} \boldsymbol{M}_{uu}^i & & \\ & \boldsymbol{M}_{vv}^i & \\ & & \boldsymbol{M}_{ww}^i \end{bmatrix}; \quad \boldsymbol{K}_i = \begin{bmatrix} \boldsymbol{K}_{uu}^i & \boldsymbol{K}_{uv}^i & \boldsymbol{K}_{uw}^i \\ \boldsymbol{K}_{uv}^{i,\mathrm{T}} & \boldsymbol{K}_{vv}^i & \boldsymbol{K}_{vw}^i \\ \boldsymbol{K}_{uw}^{i,\mathrm{T}} & \boldsymbol{K}_{vw}^{i,\mathrm{T}} & \boldsymbol{K}_{ww}^i \end{bmatrix} \quad \text{(B.2a-b)}$$

According to Reisser-Naghdi's thin shell theory, the elements of the sub-matrices $\boldsymbol{M}_i$ and $\boldsymbol{K}_i$ can be given as Eqs. (B.3a-c) and (B.4a-f), where $K = Eh/(1-\mu^2)$ and $D = Eh^3/[12\,(1-\mu^2)]$ are the membrane stiffness and bending stiffness of the shell, respectively.

For the case with the anvil included, the additional mass sub-matrix $m_c \boldsymbol{U}_{x=0}^T \boldsymbol{U}_{x=0}$ is added to the left side of the expression of $\boldsymbol{M}_{uu}^1$ which is the mass sub-matrix corresponding to the sub-shell connected to the anvil. $\boldsymbol{U}_{x=0}$ is the polynomial vector of the axial shell displacement valued at $x = 0$.

$$\boldsymbol{M}_{uu}^i = \iint_{S_i} \rho h \boldsymbol{U}^{\mathrm{T}} \boldsymbol{U} R \mathrm{d}x \mathrm{d}\theta\,,$$

$$\boldsymbol{M}_{vv}^i = \iint_{S_i} \rho h \boldsymbol{V}^{\mathrm{T}} \boldsymbol{V} R \mathrm{d}x \mathrm{d}\theta,$$

$$\boldsymbol{M}_{ww}^i = \iint_{S_i} \rho h \boldsymbol{W}^{\mathrm{T}} \boldsymbol{W} R \mathrm{d}x \mathrm{d}\theta. \quad \text{(B.3a-c)}$$

$$\boldsymbol{K}_{uu}^i = \iint_{S_i} K\left(\frac{\partial \boldsymbol{U}^{\mathrm{T}}}{\partial x}\frac{\partial \boldsymbol{U}}{\partial x} + \frac{1-\mu}{2R^2}\frac{\partial \boldsymbol{U}^{\mathrm{T}}}{\partial \theta}\frac{\partial \boldsymbol{U}}{\partial \theta}\right) R \mathrm{d}x \mathrm{d}\theta, \quad \text{(B.4a-f)}$$

$$\boldsymbol{K}_{uv}^{i}=\iint_{S_i}K(\frac{\mu}{R}\frac{\partial\boldsymbol{U}^{\mathrm{T}}}{\partial x}\frac{\partial\boldsymbol{V}}{\partial\theta}+\frac{1-\mu}{2R}\frac{\partial\boldsymbol{U}^{\mathrm{T}}}{\partial\theta}\frac{\partial\boldsymbol{V}}{\partial x})R\mathrm{d}x\mathrm{d}\theta,$$

$$\boldsymbol{K}_{uw}^{i}=\iint_{S_i}K\frac{\mu}{R}\frac{\partial\boldsymbol{U}^{\mathrm{T}}}{\partial x}\boldsymbol{W}R\mathrm{d}x\mathrm{d}\theta,$$

$$\boldsymbol{K}_{vv}^{i}=\iint_{S_i}\left[\frac{1-\mu}{2}(K+\frac{D}{R^2})\frac{\partial\boldsymbol{V}^{\mathrm{T}}}{\partial x}\frac{\partial\boldsymbol{V}}{\partial x}+\frac{1}{R^2}(K+\frac{D}{R^2})\frac{\partial\boldsymbol{V}^{\mathrm{T}}}{\partial\theta}\frac{\partial\boldsymbol{V}}{\partial\theta})\right]R\mathrm{d}x\mathrm{d}\theta,$$

$$\boldsymbol{K}_{vw}^{i}=\iint_{S_i}\left[\begin{array}{c}\frac{1}{R^2}\frac{\partial\boldsymbol{V}^{\mathrm{T}}}{\partial\theta}\left(K\boldsymbol{W}-\mu D\frac{\partial^2\boldsymbol{W}}{\partial x^2}-\frac{D}{R^2}\frac{\partial^2\boldsymbol{W}}{\partial\theta^2}\right)\\-\frac{1-\mu}{R^2}D\frac{\partial\boldsymbol{V}^{\mathrm{T}}}{\partial x}\frac{\partial^2\boldsymbol{W}}{\partial x\partial\theta}\end{array}\right]R\mathrm{d}x\mathrm{d}\theta,$$

$$\boldsymbol{K}_{ww}^{i}=\iint_{S_i}\left\{\begin{array}{c}\frac{K}{R^2}\boldsymbol{W}^{\mathrm{T}}\boldsymbol{W}\\+D\left[\begin{array}{c}\frac{\partial^2\boldsymbol{W}^{\mathrm{T}}}{\partial x^2}\frac{\partial^2\boldsymbol{W}}{\partial x^2}+\frac{\mu}{R^2}\left(\frac{\partial^2\boldsymbol{W}^{\mathrm{T}}}{\partial x^2}\frac{\partial^2\boldsymbol{W}}{\partial\theta^2}+\frac{\partial^2\boldsymbol{W}^{\mathrm{T}}}{\partial\theta^2}\frac{\partial^2\boldsymbol{W}}{\partial x^2}\right)\\+\frac{1}{R^4}\frac{\partial^2\boldsymbol{W}^{\mathrm{T}}}{\partial\theta^2}\frac{\partial^2\boldsymbol{W}}{\partial\theta^2}+\frac{2(1-\mu)}{R^2}\frac{\partial^2\boldsymbol{W}^{\mathrm{T}}}{\partial x\partial\theta}\frac{\partial^2\boldsymbol{W}}{\partial x\partial\theta}\end{array}\right]\end{array}\right\}R\mathrm{d}x\mathrm{d}\theta.$$

The stiffness matrices $\boldsymbol{K}_{\lambda}$ and $\boldsymbol{K}_{\kappa}$ can be obtained respectively by assembling the sub-matrices $\boldsymbol{K}_{\lambda}^{i,i+1}$ and $\boldsymbol{K}_{\kappa}^{i,i+1}$ which are the interface matrices between the i^{th} subshell and the $(i+1)^{\mathrm{th}}$ subshell. The interface matrix $\boldsymbol{K}_{\lambda}^{i,i+1}$ is given as

$$\boldsymbol{K}_{\lambda}^{i,i+1}=\int_0^{2\pi}\begin{bmatrix}\overline{\boldsymbol{K}}_{u_iu_i} & \overline{\boldsymbol{K}}_{u_iv_i} & \overline{\boldsymbol{K}}_{u_iw_i} & \overline{\boldsymbol{K}}_{u_iu_{i+1}} & \overline{\boldsymbol{K}}_{u_iv_{i+1}} & \boldsymbol{0}\\ \overline{\boldsymbol{K}}_{u_iv_i}^{\mathrm{T}} & \overline{\boldsymbol{K}}_{v_iv_i} & \overline{\boldsymbol{K}}_{v_iw_i} & \overline{\boldsymbol{K}}_{v_iu_{i+1}} & \overline{\boldsymbol{K}}_{v_iv_{i+1}} & \overline{\boldsymbol{K}}_{v_iw_{i+1}}\\ \overline{\boldsymbol{K}}_{u_iw_i}^{\mathrm{T}} & \overline{\boldsymbol{K}}_{v_iw_i}^{\mathrm{T}} & \overline{\boldsymbol{K}}_{w_iw_i} & \overline{\boldsymbol{K}}_{w_iu_{i+1}} & \overline{\boldsymbol{K}}_{w_iv_{i+1}} & \overline{\boldsymbol{K}}_{w_iw_{i+1}}\\ \overline{\boldsymbol{K}}_{u_iu_{i+1}}^{\mathrm{T}} & \overline{\boldsymbol{K}}_{v_iu_{i+1}}^{\mathrm{T}} & \overline{\boldsymbol{K}}_{w_iu_{i+1}}^{\mathrm{T}} & \boldsymbol{0} & \boldsymbol{0} & \boldsymbol{0}\\ \overline{\boldsymbol{K}}_{u_iv_{i+1}}^{\mathrm{T}} & \overline{\boldsymbol{K}}_{v_iv_{i+1}}^{\mathrm{T}} & \overline{\boldsymbol{K}}_{w_iv_{i+1}}^{\mathrm{T}} & \boldsymbol{0} & \boldsymbol{0} & \boldsymbol{0}\\ \boldsymbol{0} & \overline{\boldsymbol{K}}_{v_iw_{i+1}}^{\mathrm{T}} & \overline{\boldsymbol{K}}_{w_iw_{i+1}}^{\mathrm{T}} & \boldsymbol{0} & \boldsymbol{0} & \boldsymbol{0}\end{bmatrix}R\mathrm{d}\theta \tag{B.5}$$

The elements in the matrix $\boldsymbol{K}_{\lambda}^{i,i+1}$ are given by Eqs. (B.6) ~ (B.19), with $\overline{K}$ and $\overline{D}$ defined as $\overline{K}=K(1-\mu)/2$ and $\overline{D}=D(1-\mu)/2$.

$$\overline{\boldsymbol{K}}_{u_iu_i}=K\frac{\partial\boldsymbol{U}_i^{\mathrm{T}}}{\partial x}\boldsymbol{U}_i+K\boldsymbol{U}_i^{\mathrm{T}}\frac{\partial\boldsymbol{U}_i}{\partial x} \tag{B.6}$$

$$\overline{\boldsymbol{K}}_{u_iv_i}=\frac{K\mu}{R}\boldsymbol{U}_i^{\mathrm{T}}\frac{\partial\boldsymbol{V}_i}{\partial\theta}+\frac{\overline{K}}{R}\frac{\partial\boldsymbol{U}_i^{\mathrm{T}}}{\partial\theta}\boldsymbol{V}_i \tag{B.7}$$

$$\overline{\boldsymbol{K}}_{u_iw_i}=\frac{K\mu}{R}\boldsymbol{U}_i^{\mathrm{T}}\boldsymbol{W}_i \tag{B.8}$$

$$\overline{\boldsymbol{K}}_{u_i u_{i+1}} = -K\frac{\partial \boldsymbol{U}_i^{\mathrm{T}}}{\partial x}\boldsymbol{U}_{i+1} \tag{B.9}$$

$$\overline{\boldsymbol{K}}_{u_i v_{i+1}} = -\frac{\overline{K}}{R}\frac{\partial \boldsymbol{U}_i^{\mathrm{T}}}{\partial \theta}\boldsymbol{V}_{i+1} \tag{B.10}$$

$$\overline{\boldsymbol{K}}_{v_i v_i} = (\overline{K} + \frac{\overline{D}}{R^2})(\frac{\partial \boldsymbol{V}_i^{\mathrm{T}}}{\partial x}\boldsymbol{V}_i + \boldsymbol{V}_i^{\mathrm{T}}\frac{\partial \boldsymbol{V}_i}{\partial x}) \tag{B.11}$$

$$\overline{\boldsymbol{K}}_{v_i w_i} = \frac{D}{R^2}\frac{\partial^2 \boldsymbol{V}_i^{\mathrm{T}}}{\partial x \partial \theta}\boldsymbol{W}_i - \frac{\mu D}{R^2}\frac{\partial \boldsymbol{V}_i^{\mathrm{T}}}{\partial \theta}\frac{\partial \boldsymbol{W}_i}{\partial x} - \frac{2\overline{D}}{R^2}\boldsymbol{V}_i^{\mathrm{T}}\frac{\partial^2 \boldsymbol{W}_i}{\partial x \partial \theta} \tag{B.12}$$

$$\overline{\boldsymbol{K}}_{v_i u_{i+1}} = -\frac{\mu K}{R}\frac{\partial \boldsymbol{V}_i^{\mathrm{T}}}{\partial \theta}\boldsymbol{U}_{i+1} \tag{B.13}$$

$$\overline{\boldsymbol{K}}_{v_i v_{i+1}} = -(\overline{K} + \frac{\overline{D}}{R^2})\frac{\partial \boldsymbol{V}_i^{\mathrm{T}}}{\partial x}\boldsymbol{V}_{i+1} \tag{B.14}$$

$$\overline{\boldsymbol{K}}_{v_i w_{i+1}} = -\frac{D}{R^2}\frac{\partial^2 \boldsymbol{V}_i^{\mathrm{T}}}{\partial x \partial \theta}\boldsymbol{W}_{i+1} + \frac{\mu D}{R^2}\frac{\partial \boldsymbol{V}_i^{\mathrm{T}}}{\partial \theta}\frac{\partial \boldsymbol{W}_{i+1}}{\partial x} \tag{B.15}$$

$$\overline{\boldsymbol{K}}_{w_i w_i} = D\begin{bmatrix}\left(-\frac{\partial^3 \boldsymbol{W}_i^{\mathrm{T}}}{\partial x^3} - \frac{2-\mu}{R^2}\frac{\partial^3 \boldsymbol{W}_i^{\mathrm{T}}}{\partial x \partial \theta^2}\right)\boldsymbol{W}_i + \left(\frac{\partial^2 \boldsymbol{W}_i^{\mathrm{T}}}{\partial x^2} + \frac{\mu}{R^2}\frac{\partial^2 \boldsymbol{W}_i^{\mathrm{T}}}{\partial \theta^2}\right)\frac{\partial \boldsymbol{W}_i}{\partial x} \\ +\boldsymbol{W}_i^{\mathrm{T}}\left(-\frac{\partial^3 \boldsymbol{W}_i}{\partial x^3} - \frac{2-\mu}{R^2}\frac{\partial^3 \boldsymbol{W}_i}{\partial x \partial \theta^2}\right) + \frac{\partial \boldsymbol{W}_i^{\mathrm{T}}}{\partial x}(\frac{\partial^2 \boldsymbol{W}_i}{\partial x^2} + \frac{\mu}{R^2}\frac{\partial^2 \boldsymbol{W}_i}{\partial \theta^2})\end{bmatrix} \tag{B.16}$$

$$\overline{\boldsymbol{K}}_{w_i u_{i+1}} = -\frac{\mu K}{R}\boldsymbol{W}_i^{\mathrm{T}}\boldsymbol{U}_{i+1} \tag{B.17}$$

$$\overline{\boldsymbol{K}}_{w_i v_{i+1}} = \frac{2\overline{D}}{R^2}\frac{\partial^2 \boldsymbol{W}_i^{\mathrm{T}}}{\partial x \partial \theta}\boldsymbol{V}_{i+1} \tag{B.18}$$

$$\overline{\boldsymbol{K}}_{w_i w_{i+1}} = D\left(\frac{\partial^3 \boldsymbol{W}_i^{\mathrm{T}}}{\partial x^3} + \frac{2-\mu}{R^2}\frac{\partial^3 \boldsymbol{W}_i^{\mathrm{T}}}{\partial x \partial \theta^2}\right)\boldsymbol{W}_{i+1} - \left(\frac{\partial^2 \boldsymbol{W}_i^{\mathrm{T}}}{\partial x^2} + \frac{\mu}{R^2}\frac{\partial^2 \boldsymbol{W}_i^{\mathrm{T}}}{\partial \theta^2}\right)\frac{\partial \boldsymbol{W}_{i+1}}{\partial x} \tag{B.19}$$

The interface matrix $\boldsymbol{K}_{\kappa}^{i,i+1}$ introduced by the least-squares weighted residual terms between the i^{th} subshell and the $(i+1)^{\mathrm{th}}$ subshell is given as

$$\boldsymbol{K}_{\kappa}^{i,i+1} = \int_0^{2\pi}\begin{bmatrix}\widetilde{\boldsymbol{K}}_{u_i u_i} & \boldsymbol{0} & \boldsymbol{0} & \widetilde{\boldsymbol{K}}_{u_i u_{i+1}} & \boldsymbol{0} & \boldsymbol{0} \\ \boldsymbol{0} & \widetilde{\boldsymbol{K}}_{v_i v_i} & \boldsymbol{0} & \boldsymbol{0} & \widetilde{\boldsymbol{K}}_{v_i v_{i+1}} & \boldsymbol{0} \\ \boldsymbol{0} & \boldsymbol{0} & \widetilde{\boldsymbol{K}}_{w_i w_i} & \boldsymbol{0} & \boldsymbol{0} & \widetilde{\boldsymbol{K}}_{w_i w_{i+1}} \\ \widetilde{\boldsymbol{K}}_{u_i u_{i+1}}^{\mathrm{T}} & \boldsymbol{0} & \boldsymbol{0} & \boldsymbol{0} & \boldsymbol{0} & \boldsymbol{0} \\ \boldsymbol{0} & \widetilde{\boldsymbol{K}}_{v_i v_{i+1}}^{\mathrm{T}} & \boldsymbol{0} & \boldsymbol{0} & \boldsymbol{0} & \boldsymbol{0} \\ \boldsymbol{0} & \boldsymbol{0} & \widetilde{\boldsymbol{K}}_{w_i w_{i+1}}^{\mathrm{T}} & \boldsymbol{0} & \boldsymbol{0} & \boldsymbol{0}\end{bmatrix} R\mathrm{d}\theta \tag{B.20}$$

The elements in the interface matrix $\boldsymbol{K}_{\kappa}^{i,i+1}$ are given by Eqs. (B.21) ~ (B.29), with α_u, α_v, α_w and α_r being the least-squares weighted residual parameters [25].

$$\widetilde{\boldsymbol{K}}_{u_i u_i} = \kappa_u \boldsymbol{U}_i^{\mathrm{T}} \boldsymbol{U}_i \tag{B.21}$$

$$\widetilde{\boldsymbol{K}}_{u_i u_{i+1}} = -\kappa_u \boldsymbol{U}_i^{\mathrm{T}} \boldsymbol{U}_{i+1} \tag{B.22}$$

$$\widetilde{\boldsymbol{K}}_{v_i v_i} = \kappa_v \boldsymbol{V}_i^{\mathrm{T}} \boldsymbol{V}_i \tag{B.23}$$

$$\widetilde{\boldsymbol{K}}_{v_i v_{i+1}} = -\kappa_v \boldsymbol{V}_i^{\mathrm{T}} \boldsymbol{V}_{i+1} \tag{B.24}$$

$$\widetilde{\boldsymbol{K}}_{w_i w_i} = \kappa_w \boldsymbol{W}_i^{\mathrm{T}} \boldsymbol{W}_i + \kappa_r \frac{\partial \boldsymbol{W}_i^{\mathrm{T}}}{\partial x} \frac{\partial \boldsymbol{W}_i}{\partial x} \tag{B.25}$$

$$\widetilde{\boldsymbol{K}}_{w_i w_{i+1}} = -\kappa_w \boldsymbol{W}_i^{\mathrm{T}} \boldsymbol{W}_{i+1} - \kappa_r \frac{\partial \boldsymbol{W}_i^{\mathrm{T}}}{\partial x} \frac{\partial \boldsymbol{W}_{i+1}}{\partial x} \tag{B.26}$$

$$\widetilde{\boldsymbol{K}}_{u_{i+1} u_{i+1}} = \kappa_u \boldsymbol{U}_{i+1}^{\mathrm{T}} \boldsymbol{U}_{i+1} \tag{B.27}$$

$$\widetilde{\boldsymbol{K}}_{v_{i+1} v_{i+1}} = \kappa_v \boldsymbol{V}_{i+1}^{\mathrm{T}} \boldsymbol{V}_{i+1} \tag{B.28}$$

$$\widetilde{\boldsymbol{K}}_{w_{i+1} w_{i+1}} = \kappa_w \boldsymbol{W}_{i+1}^{\mathrm{T}} \boldsymbol{W}_{i+1} + \kappa_r \frac{\partial \boldsymbol{W}_{i+1}^{\mathrm{T}}}{\partial x} \frac{\partial \boldsymbol{W}_{i+1}}{\partial x} \tag{B.29}$$

Assuming that the exciting forces acting on the circumference of the pile top are, respectively, F_x in vertical direction, F_θ in circumferential direction and F_r in radial direction, the generalized force vector $\boldsymbol{F}(\omega)$ can be given as

$$\boldsymbol{F}(\omega) = \left[\boldsymbol{f}_{x_1}, \boldsymbol{f}_{\theta_1}, \boldsymbol{f}_{r_1}, \boldsymbol{0}, \boldsymbol{0}, \boldsymbol{0}, \cdots, \boldsymbol{0}, \boldsymbol{0}, \boldsymbol{0}\right]^{\mathrm{T}}, \tag{B.30}$$

where $\boldsymbol{f}_{x_1}$, $\boldsymbol{f}_{\theta_1}$, $\boldsymbol{f}_{r_1}$ are given by Eqs. (B.31) ~ (B.33). For vertical axisymmetric impact forces, $F_\theta = F_r = 0$ and the vectors $\boldsymbol{f}_{\theta_1} = \boldsymbol{f}_{r_1} = \boldsymbol{0}$.

$$\boldsymbol{f}_{x_1} = \int_0^{2\pi} \boldsymbol{U}^{\mathrm{T}} F_x R \mathrm{d}\theta \tag{B.31}$$

$$\boldsymbol{f}_{\theta_1} = \int_0^{2\pi} \boldsymbol{V}^{\mathrm{T}} F_\theta R \mathrm{d}\theta \tag{B.32}$$

$$\boldsymbol{f}_{r_1} = \int_0^{2\pi} \boldsymbol{W}^{\mathrm{T}} F_r R \mathrm{d}\theta \tag{B.33}$$

Appendix C. Coupling matrices $\boldsymbol{C_e}$, $\boldsymbol{C_i}$ and $\boldsymbol{C_{soil}}$

The sound pressure in exterior surface of the shell can be expressed in matrix form as Eq. (C.1).

$$\tilde{p}_e(x, R, \theta, \omega) = \sum_{i=1}^{I_e} \sum_{\alpha=0}^{1} \sum_{m=0}^{M} \sum_{n=0}^{\infty} \sum_{p=0}^{\infty} w_{i\alpha mn} \cdot \tilde{P}_{e,i\alpha mnp} \tag{C.1}$$

$$= [\sum_{\alpha,n,p} \tilde{P}_{e,1\alpha 1np}, \sum_{\alpha,n,p} \tilde{P}_{e,1\alpha 2np}, \cdots, \sum_{\alpha,n,p} \tilde{P}_{e,1\alpha Mnp}, \sum_{\alpha,n,p} \tilde{P}_{e,2\alpha 1np}, \cdots, \sum_{\alpha,n,p} \tilde{P}_{e,2\alpha Mnp},$$

$$\cdots, \sum_{\alpha,n,p} \tilde{P}_{e,I_e\alpha Mnp}] \cdot [w_{1\alpha 1n}, w_{1\alpha 2n}, \cdots, w_{1\alpha Mn}, w_{2\alpha 1n}, \cdots, w_{2\alpha Mn}, \cdots, w_{I_e\alpha Mn}]^{\mathrm{T}}$$

By substituting the displacement functions of the sub-shells and Eq. (C.1) into Eq. (14), the total virtual work of sound pressure on the i^{th} submerged sub-shell can be obtained as Eq. (C.2), with the sub-matrix $\widetilde{\boldsymbol{C}}_{ik}$ given in Eq. (C.3). The component term $-\delta[\mathrm{Re}(\boldsymbol{w}_i^{\mathrm{T}} e^{j\omega t}]\mathrm{Re}(\widetilde{\boldsymbol{C}}_{ik}\boldsymbol{w}_k e^{j\omega t})$ presents the virtual work done by the sound pressure contributed by the k^{th} sub-shell. Due to the presence of matrixes $\widetilde{\boldsymbol{C}}_{ik}$ and $\widetilde{\boldsymbol{C}}_{ki}$, an additional coupling relation is applied between the vibrations of the i^{th} submerged sub-shell and the k^{th} submerged sub-shell. The terms $\delta[\mathrm{Re}(\boldsymbol{w}_i^{\mathrm{T}} e^{j\omega t}]$ can be removed from the variational equation due to the randomicity of the variation. At last, the variational equation Eq. (1) is simplified to a linear equation without 2th order terms of complex variables. The global coupling matrix $\boldsymbol{C}_e$ can be obtained by assembling the sub-matrixes $\widetilde{\boldsymbol{C}}_{ik}$ together based on the arrangement of the generalized coordinate vectors as shown in Eq. (19). The derivation of the interior coupling matrix $\boldsymbol{C}_i$ is similar with that of the exterior coupling matrix.

$$\delta W_i = -\delta[\mathrm{Re}(\boldsymbol{w}_i^{\mathrm{T}} e^{j\omega t}] \cdot \mathrm{Re}\left(\int_0^{2\pi}\int_{x_i}^{x_i+1} \boldsymbol{W}^{\mathrm{T}} \cdot \mathrm{Re}(\tilde{p}_e e^{j\omega t}) R \mathrm{d}x\, \mathrm{d}\theta\right) \tag{C.2}$$

$$= -\delta[\mathrm{Re}(\boldsymbol{w}_i^{\mathrm{T}} e^{j\omega t}]$$

$$\cdot \mathrm{Re}\left\{\int_0^{2\pi}\int_{x_i}^{x_i+1}\left(\begin{array}{c}\boldsymbol{W}^{\mathrm{T}} \cdot [\sum_{\alpha,n,p} \tilde{P}_{e,1\alpha 1np}, \sum_{\alpha,n,p} \tilde{P}_{e,1\alpha 2np}, \cdots, \sum_{\alpha,n,p} \tilde{P}_{e,1\alpha Mnp},\\ \sum_{\alpha,n,p} \tilde{P}_{e,2\alpha 1np}, \cdots, \sum_{\alpha,n,p} \tilde{P}_{e,2\alpha Mnp}, \cdots, \sum_{\alpha,n,p} \tilde{P}_{e,I_e\alpha Mnp}] \cdot R \mathrm{d}x\end{array}\right)\mathrm{d}\theta\right\}$$

$$\cdot \left[w_{1\alpha 1n}, w_{1\alpha 2n}, \cdots, w_{1\alpha Mn}, w_{2\alpha 1n}, \cdots, w_{2\alpha Mn}, \cdots, w_{I_e\alpha Mn}\right]^{\mathrm{T}} e^{j\omega t}$$

$$= -\delta[\mathrm{Re}(\boldsymbol{w}_i^{\mathrm{T}} e^{j\omega t}] \cdot \mathrm{Re}\left\{\left[\widetilde{\boldsymbol{C}}_{i1}, \widetilde{\boldsymbol{C}}_{i2}, \cdots, \widetilde{\boldsymbol{C}}_{iI_e}\right] \cdot \left[\boldsymbol{w}_1^{\mathrm{T}}, \boldsymbol{w}_2^{\mathrm{T}}, \cdots, \boldsymbol{w}_{I_e}^{\mathrm{T}}\right]^{\mathrm{T}} e^{j\omega t}\right\}, \qquad (1 \le i \le I_e)$$

$$\widetilde{\boldsymbol{C}}_{ik} = \int_0^{2\pi}\int_{x_i}^{x_i+1}\left(\begin{array}{c}\boldsymbol{W}^{\mathrm{T}} \cdot [\sum_{\alpha,n,p} \tilde{P}_{e,k\alpha 1np}, \sum_{\alpha,n,p} \tilde{P}_{e,k\alpha 2np},\\ \cdots, \sum_{\alpha,n,p} \tilde{P}_{e,k\alpha Mnp}] R \mathrm{d}x\end{array}\right)\mathrm{d}\theta, \qquad (1 \le k \le I_e) \tag{C.3}$$

Provided that the minimum and maximum vertical coordinates of the pile-soil contact surface on a sub-shell are x_{s1} and x_{s2}, respectively. By substituting displacement functions ($u = \boldsymbol{U} \cdot \boldsymbol{u} e^{j\omega t}$, $v = \boldsymbol{V} \cdot \boldsymbol{v} e^{j\omega t}$, $w = \boldsymbol{W} \cdot \boldsymbol{w} e^{j\omega t}$) into Eq. (15) and (16), the virtual works done by the springs and dashpots can be given as Eq. (C.4) and (C.5), respectively. Therefore, the additional term incorporated into the governing equation can be expressed as Eq. (C.6), with its sub-matrices given in Eq. (C.7a-c) and (C.8a-c). The global coupling matrix $\boldsymbol{C}_{\mathrm{soil}}$ can be obtained by assembling the matrixes $\boldsymbol{C}_{s0}$ together.

$$\delta W_{\text{spring}} = -\delta[\text{Re}(\boldsymbol{u}^{\text{T}}e^{j\omega t})] \cdot \text{Re}\left(\int_0^{2\pi}\int_{x_{s1}}^{x_{s2}} k_x \boldsymbol{U}^{\text{T}}\boldsymbol{U}R\text{d}x\text{d}\theta \cdot \boldsymbol{u}e^{j\omega t}\right) - \delta[\text{Re}(\boldsymbol{v}^{\text{T}}e^{j\omega t})]\text{Re}\left(\int_0^{2\pi}\int_{x_{s1}}^{x_{s2}} k_\theta \boldsymbol{V}^{\text{T}}\boldsymbol{V}R\text{d}x\text{d}\theta \cdot \boldsymbol{v}e^{j\omega t}\right) - \delta[\text{Re}(\boldsymbol{w}^{\text{T}}e^{j\omega t})]\text{Re}\left(\int_0^{2\pi}\int_{x_{s1}}^{x_{s2}} k_r \boldsymbol{W}^{\text{T}}\boldsymbol{W}R\text{d}x\text{d}\theta \cdot \boldsymbol{w}e^{j\omega t}\right), \tag{C.4}$$

$$\delta W_{\text{dashpot}} = -\delta[\text{Re}(\boldsymbol{u}^{\text{T}}e^{j\omega t})]\text{Re}\left(\int_0^{2\pi}\int_{x_{s1}}^{x_{s2}} j\omega c_x \boldsymbol{U}^{\text{T}}\boldsymbol{U}R\text{d}x\text{d}\theta \cdot \boldsymbol{u}e^{j\omega t}\right) - \delta[\text{Re}(\boldsymbol{v}^{\text{T}}e^{j\omega t})]\text{Re}\left(\int_0^{2\pi}\int_{x_{s1}}^{x_{s2}} j\omega c_\theta \boldsymbol{V}^{\text{T}}\boldsymbol{V}R\text{d}x\text{d}\theta \cdot \boldsymbol{v}e^{j\omega t}\right) - \delta[\text{Re}(\boldsymbol{w}^{\text{T}}e^{j\omega t})]\text{Re}\left(\int_0^{2\pi}\int_{x_{s1}}^{x_{s2}} j\omega c_r \boldsymbol{W}^{\text{T}}\boldsymbol{W}R\text{d}x\text{d}\theta \cdot \boldsymbol{w}e^{j\omega t}\right), \tag{C.5}$$

$$j\omega \boldsymbol{C}_{s0}\begin{bmatrix}\boldsymbol{u}\\ \boldsymbol{v}\\ \boldsymbol{w}\end{bmatrix} = j\omega\begin{bmatrix}\frac{\boldsymbol{K}_{uu}}{j\omega}+\boldsymbol{C}_{uu} & \boldsymbol{0} & \boldsymbol{0}\\ \boldsymbol{0} & \frac{\boldsymbol{K}_{vv}}{j\omega}+\boldsymbol{C}_{vv} & \boldsymbol{0}\\ \boldsymbol{0} & \boldsymbol{0} & \frac{\boldsymbol{K}_{ww}}{j\omega}+\boldsymbol{C}_{ww}\end{bmatrix}\begin{bmatrix}\boldsymbol{u}\\ \boldsymbol{v}\\ \boldsymbol{w}\end{bmatrix} \tag{C.6}$$

$$\boldsymbol{K}_{uu} = k_x\int_0^{2\pi}\int_{x_{s1}}^{x_{s2}} \boldsymbol{U}^{\text{T}}\boldsymbol{U}R\text{d}x\text{d}\theta \tag{C.7a-c}$$

$$\boldsymbol{K}_{vv} = k_\theta\int_0^{2\pi}\int_{x_{s1}}^{x_{s2}} \boldsymbol{V}^{\text{T}}\boldsymbol{V}R\text{d}x\text{d}\theta$$

$$\boldsymbol{K}_{ww} = k_r\int_0^{2\pi}\int_{x_{s1}}^{x_{s2}} \boldsymbol{W}^{\text{T}}\boldsymbol{W}R\text{d}x\text{d}\theta$$

$$\boldsymbol{C}_{uu} = c_x\int_0^{2\pi}\int_{x_{s1}}^{x_{s2}} \boldsymbol{U}^{\text{T}}\boldsymbol{U}R\text{d}x\text{d}\theta \tag{C.8a-c}$$

$$\boldsymbol{C}_{vv} = c_\theta\int_0^{2\pi}\int_{x_1}^{x_{s2}} \boldsymbol{V}^{\text{T}}\boldsymbol{V}R\text{d}x\text{d}\theta$$

$$\boldsymbol{C}_{ww} = c_r\int_0^{2\pi}\int_{x_{s1}}^{x_{s2}} \boldsymbol{W}^{\text{T}}\boldsymbol{W}R\text{d}x\text{d}\theta$$

References

[1] P.T. Madsen, M. Wahlberg, J. Tougaard, K. Lucke, P. Tyack, Wind turbine underwater noise and marine mammals: implications of current knowledge and data needs, Marine Ecology-Progress Series, 309 (2006) 279-295.

[2] H. Slabbekoorn, N. Bouton, I. van Opzeeland, A. Coers, C. ten Cate, A.N. Popper, A noisy spring: The impact of globally rising underwater sound levels on fish, Trends in Ecology and Evolution, 25 (2010) 419-427.

[3] T.A. Jefferson, S.K. Hung, B. Wursig, Protecting small cetaceans from coastal development: Impact assessment and mitigation experience in Hong Kong, Marine Policy, 33 (2009) 305-311.

[4] P.R. Stepanishen, Radiated power and radiation loading of cylindrical surfaces with nonuniform velocity distributions, The Journal of the Acoustical Society of America, 63 (1978) 328-338.

[5] P.R. Stepanishen, MODAL COUPLING IN THE VIBRATION OF FLUID-LOADED CYLINDRICAL SHELLS, Journal of the Acoustical Society of America, 71 (1982) 813-823.

[6] B. Laulagnet, J.L. Guyader, Modal analysis of a shell's acoustic radiation in light and heavy fluids, Journal of Sound and Vibration, 131 (1989) 397-415.

[7] M. Caresta, N.J. Kessissoglou, Structural and acoustic responses of a fluid-loaded cylindrical hull with structural discontinuities, Applied Acoustics, 70 (2009) 954-963.

[8] M. Caresta, N.J. Kessissoglou, Acoustic signature of a submarine hull under harmonic excitation, Applied Acoustics, 71 (2010) 17-31.

[9] M.K. Kwak, J.-R. Koo, C.-H. Bae, Free vibration analysis of a hung clamped-free cylindrical shell partially submerged in fluid, Journal of Fluids and Structures, 27 (2011) 283-296.

[10] M.K. Au-Yang, Dynamics of Coupled Fluid-Shells, Journal of Vibration and Acoustics, 108 (1986) 339-347.

[11] F.J. Fahy, P. Gardonio, Sound and Structural Vibration: Radiation, Transmission and Response, Elsevier Science, 2007.

[12] M.C. Junger, D. Feit, Sound, Structures, and Their Interaction, MIT Press, 1986.

[13] M.P. Païdoussis, G.X. Li, Pipes Conveying Fluid: A Model Dynamical Problem, Journal of Fluids and Structures, 7 (1993) 137-204.

[14] P.G. Reinhall, P.H. Dahl, Acoustic radiation from a submerged pile during pile driving, 2010 Oceans Mts/Ieee Seattle, (2010).

[15] M. Zampolli, M.J.J. Nijhof, C.A.F. de Jong, M.A. Ainslie, E.H.W. Jansen, B.A.J. Quesson, Validation of finite element computations for the quantitative prediction of underwater noise from impact pile driving, The Journal of the Acoustical Society of America, 133 (2013) 72-81.

[16] P.G. Reinhall, P.H. Dahl, Underwater Mach wave radiation from impact pile driving: Theory and observation, The Journal of the Acoustical Society of America, 130 (2011) 1209-1216.

[17] H. Kim, G.R. Potty, J.H. Miller, K.B. Smith, G. Dossot, Long range propagation modeling of offshore wind turbine noise using finite element and parabolic equation models, The Journal of the Acoustical Society of America, 131 (2012) 3392-3392.

[18] T. Lippert, S. Lippert, O.v. Estorff, Prediction of Pile Driving Induced Underwater Noise, 19th International Congress on Sound and Vibration, (2012).

[19] T. Lippert, O. von Estorff, The significance of parameter uncertainties for the prediction of offshore pile driving noise, The Journal of the Acoustical Society of America, 136 (2014) 2463-2471.

[20] M.B. Fricke, R. Rolfes, Towards a complete physically based forecast model for underwater noise related to impact pile driving, The Journal of the Acoustical Society of America, 137 (2015) 1564-1575.

[21] M.V. Hall, A semi-analytical model for non-Mach peak pressure of underwater acoustic pulses from offshore pile driving, Acoustics Australia, 41 (2013) 43.

[22] M.V. Hall, An analytical model for the underwater sound pressure waveforms radiated when an offshore pile is drivena), The Journal of the Acoustical Society of America, 138 (2015) 795-806.

[23] A. Tsouvalas, A.V. Metrikine, A semi-analytical model for the prediction of underwater noise from offshore pile driving, Journal of Sound and Vibration, 332 (2013) 3232-3257.

[24] A.W. Leissa, Vibration of shells, Scientific and Technical Information Office, National Aeronautics and Space Administration, 1973.

[25] Y.G. Qu, Y. Chen, X.H. Long, H.X. Hua, G. Meng, Free and forced vibration analysis of uniform and stepped circular cylindrical shells using a domain decomposition method, Applied Acoustics, 74 (2013) 425-439.

[26] Y.G. Qu, H.X. Hua, G. Meng, A domain decomposition approach for vibration analysis of isotropic and composite cylindrical shells with arbitrary boundaries, Composite Structures, 95 (2013) 307-321.

[27] A. Jeffrey, H.H. Dai, Handbook of Mathematical Formulas and Integrals, Elsevier Science, 2008.

[28] C.G. Don, A.J. Cramond, Soil impedance measurements by an acoustic pulse technique, The Journal of the Acoustical Society of America, 77 (1985) 1601-1609.

[29] G. Gazetas, R. Dobry, Simple Radiation Damping Model for Piles and Footings, Journal of Engineering Mechanics, 110 (1984) 937-956.

[30] G. Gazetas, R. Dobry, Horizontal Response of Piles in Layered Soils, Journal of Geotechnical Engineering, 110 (1984) 20-40.

[31] A.J. Deeks, M.F. Randolph, Analytical modelling of hammer impact for pile driving, International Journal for Numerical and Analytical Methods in Geomechanics, 17 (1993) 279-302.

[32] W.A. Take, A.J. Valsangkar, M.F. Randolph, Analytical solution for pile hammer impact, Computers and Geotechnics, 25 (1999) 57-74.

[33] IHC Foundation Equipment, IHCWave Stress Wave Package Version 1.3.2001-10, in, IHC Merwede, Kinderdijk, The Netherlands, 2001, pp. IHC Merwede, Kinderdijk, The Netherlands, 2001.

[34] H.S. Gill, Control of impact pile driving noise and study of alternative techniques, Noise Control Engineering Journal, 20 (1983) 76-83.

[35] W.A. Take, A.J. Valsangkar, M.F. Randolph, Analytical solution for pile hammer impact, Computers and Geotechnics, 25 (1999) 57-74.

[36] J.L. Briaud, Geotechnical Engineering: Unsaturated and Saturated Soils, Wiley, 2013.

List of figure captions

Fig. 1. Pile-driving model